Scramjet Flow Field Control Using Magnetogasdynamics

AFOSR FINAL REPORT

Richard J. McMullan, Major, USAF

DEPARTMENT OF THE AIR FORCE
AIR UNIVERSITY

AIR FORCE INSTITUTE OF TECHNOLOGY

Wright-Patterson Air Force Base, Ohio

Scramjet Flow Field Control Using Magnetogasdynamics

AFOSR FINAL REPORT

Department of Aeronautical and Astronautical Engineering

Graduate School of Engineering and Management

Air Force Institute of Technology

Air University

Air Education and Training Command

Richard J. McMullan

Major, USAF

April 2006

Abstract

Sustained hypersonic flight using scramjet propulsion is the key technology bridging the gap between turbojets and the exoatmospheric environment where a rocket is required. Recent efforts have focused on electromagnetic (EM) flow control to mitigate the problems of high thermomechanical loads and low propulsion efficiencies associated with scramjet propulsion. Numerical simulations were employed to determine how EM flow control can improve scramjet performance. The research effort focused on applying both local flow field control and the system level magnetogasdynamic (MGD) energy bypass method to a flight-scale scramjet. This report highlights the major accomplishments of this research effort. Combustor-based MGD generators proved superior to inlet generators with respect to power density and overall engine efficiency. MGD acceleration was shown to be ineffective in improving overall performance with all of the bypass engines having approximately 33% more drag than baseline engine without EM flow control, and none of them achieved a self-powered state.

Acknowledgements

Table of Contents

List of Figures

Figure   Page

List of Tables

List of Symbols

Symbol		Page

List of Abbreviations

Scramjet Flow Field Control Using Magnetogasdynamics

I. Introduction

1.1 Scramjet Operation, Design Challenges, and a Brief History

Jet engines of all varieties depend on the compression of ambient air to provide the oxidizer needed for combustion. A ramjet compresses the ambient air entirely through deceleration of the freestream flow, typically by one or more inlet shockwaves. The ram compression process is one of conversion of freestream kinetic energy to internal energy as manifested by increased temperature, pressure, and density and lower relative Mach number. Ramjets are most efficient when operated in a freestream regime of approximately Mach 3 - 6. At speeds approaching Mach 6, the aerodynamic losses (e.g. total pressure, drag), heating, and increased structural requirements that accompany compression of the flow to subsonic combustion speeds render the ordinary ramjet excessively inefficient. Thus, to extend the airbreathing performance envelope to higher Mach numbers, supersonic combustion has been pursued.

The supersonic combustion ramjet, or scramjet, is by definition then a ramjet engine where the entire combustion process occurs under locally supersonic conditions. A typical scramjet flowpath as shown in Figure 1.1 can be distinguished by three primary processes: compression, combustion, and expansion. First, the freestream air is compressed externally and/or internally. This is usually accomplished by a series of oblique shockwaves but may also include isentropic compression. The goal of the compression process is to attain high enough static pressure to sustain combustion while minimizing aerodynamic losses and limiting the static temperature increase. The second limitation is necessary to minimize flow energy losses due to molecular vibration and dissociation. Combustion heat release then increases the flow energy which is exchanged for an overall flow momentum increase through an expansion process, producing net positive thrust. For such a simple thermodynamic process,

several formidable technical issues have precluded a scramjet-powered flight vehicle until quite recently.
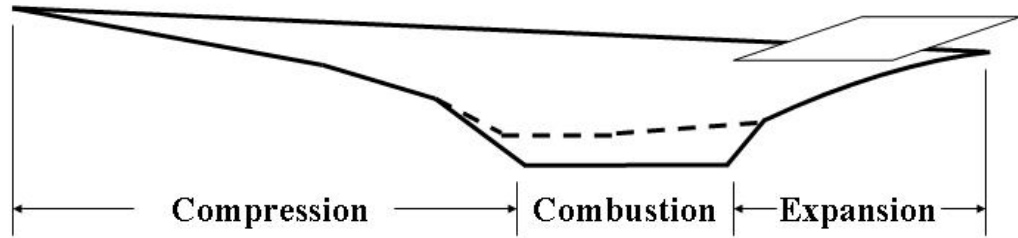
Figure 1.1:   Typical Scramjet Engine Schematic

NASA's X-43 program began in the late 1990s and, with its successful flight test in March 2004, currently represents the state-of-the-art in scramjet propulsion [6]. The X-43A uses a hydrogen-fueled scramjet engine which is highly integrated with the airframe. This flight demonstration vehicle is released from a B-52 and accelerated to flight test conditions by the first stage of a Pegasus expendable launch vehicle. Upon reaching these conditions, the X-43 is released from its booster and is then self-propelled by its scramjet engine. On 27 March 2004, the vehicle became the first scramjet device to demonstrate net thrust [8] and set a world speed record for airbreathing aircraft with its 11 second flight at Mach 6.83 and 100,000 feet [37]. By 16 November 2004, a second X-43A pushed the speed record even further, achieving Mach 9.6 during a 10-second burn of its engine after being "boosted to an altitude of 33,223 meters (109,000 feet) by a Pegasus rocket launched from beneath a B52-B jet aircraft." [38]

Although a great milestone has been reached with the X-43, broad technical challenges remain. Of these, the greatest issues are thermal control, maximizing component and system efficiencies and achieving adequate fuel mixing and combustion within typical combustor residence times measured in milliseconds. Various flow control mechanisms have been proposed, especially with respect to better conditioning of the flow entering the combustor. As a final issue, there is much uncertainty in the

scaling of an X-43 type flight demonstrator into the design of an operational flight vehicle.

1.2   A Review of Magnetogasdynamic Flow Control Concepts

As far back as the 1960s, practical magnetogasdynamic (MGD) applications were studied in earnest, not only for terrestrial electrical power generation [45] but also for electrical propulsion and aerodynamic control [49]. Magnetogasdynamics (also referred to as magnetohydrodynamics or magnetofluidmechanics by various authors) is broadly defined by Hughes and Young in their seminal textbook as "the study of the flow of electrically conducting fluids in the presence of a magnetic field under certain special assumptions [18]." In short, the fluid flow is coupled to Maxwell's equations for electromagnetism through an electromagnetic body force known as the Lorentz Force and its associated energy interaction. In the infancy of hypersonic flight, it was recognized that the air within the hypersonic shock layer surrounding the vehicle could become appreciably ionized. This fact "prompted research on methods of magnetically interacting with the flow to produce various effects, including control of drag or angle of attack, and boundary-layer control to increase the transition Reynolds number or to reduce the hypersonic heat transfer" [49]. Recent experimental and numerical research efforts have focused on internal MGD flow control and electrical power generation (i.e. within scramjet engines) as well as the external aerodynamics, with key goals being the mitigation of the high thermomechanical loads and low propulsion efficiencies.

Recent MGD flow control efforts have ranged from basic scientific exploration of the concept to simple analytical and experimental applications. A good example of the former is the MGD flow characterization conducted in the Mach 3 and Mach 4 plasma tunnels at The Ohio State University (OSU) [33, 35, 39]. These experiments are investigating basic unit problems specifically relevant to MGD flow control by exploring three-dimensional supersonic flow in a channel. Specific work at this facility has sought to attain and characterize a sustainable, non-equilibrium plasma. Various approaches using high intensity radio frequency (RF) discharges have been taken to

accomplish this ionization. Flowing nitrogen at Mach 3 through a 3-cm wide test section, a sustained RF discharge at 1kW was capable of achieving a conductivity of 0.24mho/m in the presence of a magnetic field of 1.5 Tesla (T). From the standpoint of required ionization power, a more efficient approach demonstrated a pulsed-RF signal with a 20ns duration and 40kHz repetition rate with a peak power approaching 1MW. When combined with a sustaining direct current electric field, both air and nitrogen Mach 4 flows produced uniform, stable plasmas with conductivities of 0.09mho/m and 0.18mho/m, respectively.

Complementing this basic scientific exploration, a significant amount of analytical work exists with respect to both creating/sustaining a non-equilibrium plasma as well as putting this plasma to work through MGD interaction. However, it should be immediately noted that in order to make most practical analytical problems tractable, significant simplifying assumptions must be made. For example, the analytical work described in the remainder of this section was either 1D or 2D and assumed inviscid flow. Furthermore, except for some of the electron ionization models, chemical composition is assumed fixed, and typically the assumption of a calorically perfect gas is made. With this in mind, a large body of work to this effect has been produced by Macheret and associates at Princeton University. In 1997, they proposed using a 30keV electron beam to ionize a Mach 10.6 wind tunnel flow and then use the Lorentz force to accelerate the flow to Mach 14.3 [27]. In 2001 and 2002, they put forward several detailed papers focused on non-equilibrium ionization methods with application toward supersonic MGD power generation. Two years prior to the OSU work described above, they explored both electron beams and steady and pulsed electric fields, concluding high energy electron beams (order of 10–1000s of eV) required 1-2 orders of magnitude lower input power than a comparable ionization produced by an electric field [31]. Applying this conclusion to a simplified 2D analysis of a MGD-controlled scramjet inlet, they predicted the ability to maintain the shock-on-cowl-lip condition for Mach numbers of two greater than the geometrical design Mach number [30]. Although some of this effect was attributable to heating, the work done by

the Lorentz force was shown to be a significant contributor as well. This same work also demonstrated more electrical power was generated by the MGD interaction than was required to power the electron beam ionization source. Similar calculations for a 3x0.25x0.25-meter inlet at flight Mach numbers of 4–10, subjected to a 7T magnetic field, generated several MW of excess power by converting approximately 1/3 of the flow enthalpy to electrical power [28, 29]. In the past two years, 1D and 2D analytical work has predicted MW-class power generation using more moderate 1T magnetic fields in potassium-seeded combustor flows; power that would then be made available for applications such as the control of inlet shock location using virtual cowl shapes created by MGD and/or plasma-controlled external combustion [32, 47, 48]. Finally, recent research has extended these concepts to wind tunnel models of simple aerodynamic structures [2] providing evidence to support the basic science and analytical work and reinforcing the need to continue exploration of flight vehicle-sized applications such as the MGD-energy bypass discussed next.

The most ambitious overall MGD system application is without a doubt the MGD-energy bypass method which has been examined in several contexts by multiple researchers [5, 11, 26, 34, 40, 44]. However, the most frequently cited example of the application of an MGD energy bypass method remains that originally espoused by Russian researchers led by A.L. Kuranov at the Hypersonic Systems Research Institute (HSRI) in St. Petersburg. HSRI researchers developed a conceptual hypersonic aircraft, known as AJAX, which relied on their Magneto-Plasma Chemical Engine (MPCE) for both power and propulsion [3, 4, 21]. The conceptual work on the AJAX vehicle was among the first to show the potential for electromagnetic-fluid interactions to improve the performance of scramjet engines. Specific to the AJAX approach was the use of a parameter-based quasi-1D analysis (as well 2D inlet-specific numerical studies). This analysis utilized the inviscid subset of the Navier-Stokes fluid flow equations (i.e. the Euler equations) coupled to a source term formulation of Maxwell's equations for electromagnetic fields [21]. The latter equations were cast in terms of the applied magnetic flux density, $\vec{B}$, the load factor, k, and a scalar

electrical conductivity, σ. In addition, the model assumed a calorically perfect gas existed throughout the flow. A final, critical supposition was that the flow sustained a level of ionization sufficient to ensure appreciable MGD interaction. Assuming all of the enthalpy extracted from the flow was made available to the MGD accelerator, the MPCE was shown in some cases to produce 5-10 percent higher specific impulse (I_{SP}) than a conventional scramjet of the same geometry when approximately 10 percent of the freestream enthalpy was extracted from the flow. Further studies defined the self-powered MGD bypass system envelope for a Mach 6 engine in terms of the magnetic field, ionization power and relative effectiveness of the electromagnetic interaction [20]. In this model, self-powered operation was attained for magnetic fields stronger than about 0.8T when the ionization power was on the order of 2W/cm^3. As pointed out by the authors' conclusions though, the "extent of magnetohydrodynamic (MHD) influence on scramjet performance essentially depends on the type of MHD generator, inlet characteristics, load factors, Hall parameter, ionizer parameters, and flow parameters [19]."

Regarding the components of a typical MGD bypass system, Figure 1.2 presents a simplified schematic of the MPCE with its key features. One or more MGD generators perform two key functions. First, a portion of the freestream enthalpy is extracted and converted to electrical power, and second, more efficient flow compression is obtained than through the use of shock-trains alone [19, 50]. A portion of the extracted electricity is used to power a flow ionization system, which for AJAX was always assumed to be accomplished by a high energy electron beam source [22] described in greater detail in Section 2.5. The remaining electrical energy is available for onboard electrical power requirements to include the use of an MGD accelerator, if desired. The MGD accelerator is installed downstream of the combustion chamber to convert electrical energy back into flow enthalpy, thereby increasing the thrust. In the work referenced here, all power left over after flow ionization, which varied anywhere from 0.0 to 100W/cm^3 was returned as flow enthalpy in an MGD accelerator [22]. Bypassing a portion of the inlet flow energy around the combustor in this manner,
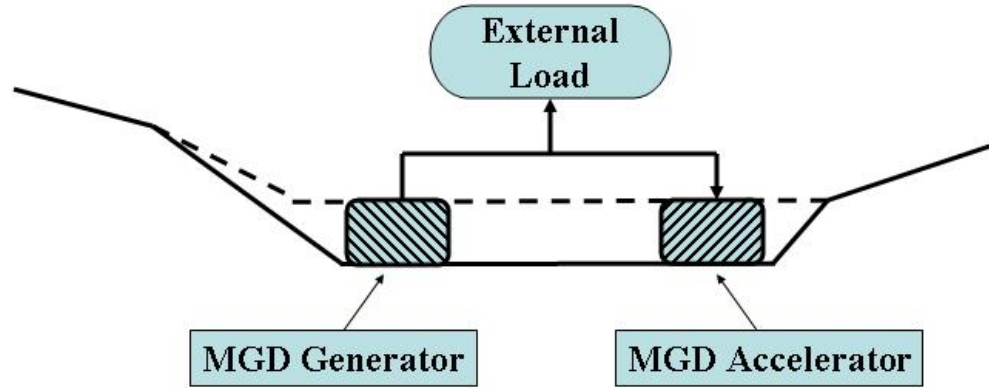
Figure 1.2:   Magneto-Plasma Chemical Engine (MPCE) Schematic

may also also allow the combustor to operate more efficiently. This is possible because the flow enters the combustor of an MGD bypass equipped scramjet at both higher pressure and lower Mach number.

1.3   Magnetogasdynamic Flow Control Research Foundation

Inspired in part by AJAX and related efforts, Air Force Research Laboratory (AFRL) researchers extended the capability to analyze MGD flow control applications by developing a computational fluid dynamics (CFD) code to model the full, three-dimensional set of coupled Navier-Stokes and Maxwell's equations for a non-ideal gas [10]. (As an aside, 'non-ideal' in this context refers to the non-uniform conductivity found in the weakly ionized, less than perfectly conducting fluid typical of the altitudes and low hypersonic Mach numbers encountered by scramjets.) However, the code did not address chemical kinetics but instead relied on a calorically perfect gas model.

The first AFRL studies examined external flows around hypersonic blunt bodies, specifically an axisymmetric, spherical-nosed body with an imposed magnetic dipole field [41]. The numerical results compared well with the analytical solution. First, it was shown for the levels of thermal ionization typical of reentry ($\sim$100mho/m) that magnetic flux densities greater than 1T could slow the flow in the shock layer,

1-7

increase drag, and increase the shock standoff distance. Then the same fields were demonstrated to lower the wall heat flux in the stagnation point region, an effect that increased with increasing magnetic field and decreased whenever the electrical conductivity was non-ideal [42, 43].

Having developed an approach to handle the full equation set, including the generalized diffusivity terms, efforts commenced to increase the fidelity and efficiency of the code [13]. The MGD approximations are ideally suited for the hypersonic flows of practical interest to scramjet design. This is because they are certainly non-relativistic and occur at sufficient dynamic pressure to maintain the gas as a dense, collision-dominated plasma. The latter property ensures that although the plasma is conductive, the high frequency of collisions promote both ionization and recombination, keeping both charge separation and the conductivity relatively small (what is referred to commonly as a *weakly ionized* plasma). Under these conditions, if the MGD interaction is to be appreciable, the applied magnetic field has to be relatively large to make up for the low conductivity. In fact, the applied magnetic field significantly influences the fluid motion. However, the flow distorts the induced magnetic field which is assumed to be relatively small compared to the externally applied field. This set of circumstances is embodied in the low Re_m condition which is expressed mathematically by Equation 1.1 where V_0, L_0, σ_0, and μ_e are the reference values for velocity, length, conductivity, and magnetic permeability, respectively. As an example, a one meter nose radius blunt body, flying at 8 km/s at an altitude of 61 km would produce only $\sigma = 300$ mho/m in the equilibrium flow downstream of the bow shock, resulting in $Re_m \sim 3$ [42]. This example corresponds to a re-entry vehicle at a Mach number (M) greater than 20. At the lower altitudes and Mach numbers envisioned for scramjets, $Re_m << 1$ is a valid assumption.

$$Re_m = V_0 L_0 \sigma_0 \mu_e \tag{1.1}$$

The conclusion to be drawn from the combination of low σ and high $\vec{B}$ that defines the low Re_m regime is that electromagnetic effects may be added directly to the Navier-Stokes equations as simple source terms. This approach proved conducive to allowing traditional upwind spatial discretization schemes such as the Roe flux difference scheme that, while lower in order of spatial accuracy, were much less diffusive in capturing flow discontinuities such as shocks. A Poisson solver was then incorporated to provide the option of either calculating the electric field, $\vec{E}$, or simply specifying its vector components at every point [14]. When taking the former, higher fidelity, approach, the scalar electric potential, ϕ, on the boundaries is specified and subsequently $\vec{E} = -\nabla \phi$ is solved by enforcing current continuity as given by Equation 1.2 where the conduction current, $\vec{j}$, is given by Ohm's Law in the form of Equation 1.3. (In Equation 1.3, $\vec{V}$ is the velocity and the other variables are as previously defined.) As an aside, the generalized Ohm's law can be applied to account for the Hall effect and ion-slip typically encountered in flows with extremely high applied magnetic fields [13]. However, in this research, Hall Effect was not factored into the results.

$$\nabla \cdot \vec{j} = 0 \tag{1.2}$$

$$\vec{j} = \sigma \left[\vec{E} + \vec{V} \times \vec{B} \right] \tag{1.3}$$

Finally, two more tools were added to the method, the first to improve stability and the second to address turbulent flows. Regarding the former, an approximately-factored Beam-Warming implicit method was developed to overcome the time-step stability limitation of the previously used 4th order Runge-Kutta (RK4) scheme that was encountered, especially when using highly stretched meshes [13]. The implicit method, while limited to second-order accuracy, demonstrated several important advantages. These advantages were demonstrated on two sample problems of electromagnetic field diffusion and wave propagation which were also solved analytically and with the explicit RK4 scheme. Both computational methods compared well with the

1-9

analytical solution, however the implicit method had a stable time step size three orders of magnitude greater than the RK4 scheme, and each implicit time step required only 5% more computational time than its explicit counterpart. As far as turbulent flows were concerned, the magnetic field's impact on turbulence presented a significant challenge. This is due primarily to the anisotropy brought about the preferential damping of turbulent fluctuations normal to the magnetic field [46]. Therefore, an engineering-based approach using a two equation $k - \epsilon$ turbulence model based on liquid metal flows was incorporated to "mimic some of the anticipated effects of the magnetic field in a simple yet effective manner [13]." The $k - \epsilon$ equations are also integrated implicitly in time but are loosely coupled to the flow equations. This loose coupling considerably reduces the expense of computing the flux Jacobians. Several calculations of turbulent flow over a flat plate were made to characterize the effect of a transverse magnetic field on the flow. Among other things, decreases in the local skin friction coefficient in the vicinity of the magnetic dipole were observed. In addition, it was "evident that in the context of the present model the dominant effect of the magnetic field is on the interaction with the mean flow" [13] as demonstrated by a thickening of the boundary layer and corresponding reduction in surface gradient. Having all of these tools, the code was sufficiently developed to attempt modelling problems of practical engineering interest.

With the code matured and verified, the first ever attempt was made to numerically model an entire 3D scramjet flowpath to "explore the fluid dynamics of scramjet internal flows, and their interaction with a specified plasma and combustion environment [11]." The electromagnetic source term form of the governing equations was used with combustion accounted for by a volumetric heating rate source term in the energy equation. Both laminar and turbulent cases were explored. Using freestream reference conditions for the Reynold's number (Re), Mach number (M), and temperature (T), respectively, of $Re = 1.6 \times 10^6$, $M_0 = 8.0$ and $T_0 = 250$K, the flowpath, as shown in Fig 1.3, began with a dual-plane compression system with an MGD generator in the horizontal compression surface. This was followed by a combined,

constant-area isolator and combustor, and finally a two ramp internal/external expansion surface. This model geometry was intentionally simplified to prevent adverse effects like thermal choking, and no attempt at performance optimization was made. Modelling simplifications were made to allow for the fact that detailed ionization and thermochemistry models were not part of the code. In effect, flow conductivity and combustion heat addition were modelled using Gaussian distributions that were placed in the inlet/exit and combustor, respectively [11].
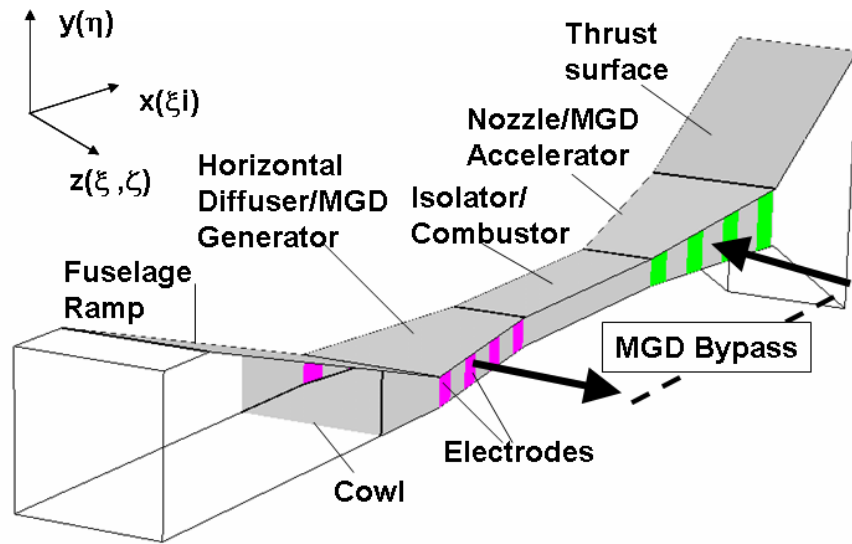
Figure 1.3:   AFRL/VA Scramjet Model [21]

Even with these simplifications and assumptions, sometimes unexpected results were obtained [11]. For example, the 3D viscous interaction effects altered the structure of the current and Lorentz fields in the MGD component regions. Vortical structures due to the sidewall compression (readily evident in Figure 1.4(a)) also gave rise to several non-uniform current features in the flow. Several of these features can be seen in Figure 1.4(b) such as the eddy currents and current 'pinch' in the inlet. In the boundary layer, the applied $\vec{E}$-field exceeded that induced by the flow motion $(\vec{V} \times \vec{B})$ causing the local reversal of the current and Lorentz Force (e.g. flow acceleration vice deceleration in the MGD generator). Finally, spanwise (i.e. yawing) force components were observed, although the geometry was symmetric about the
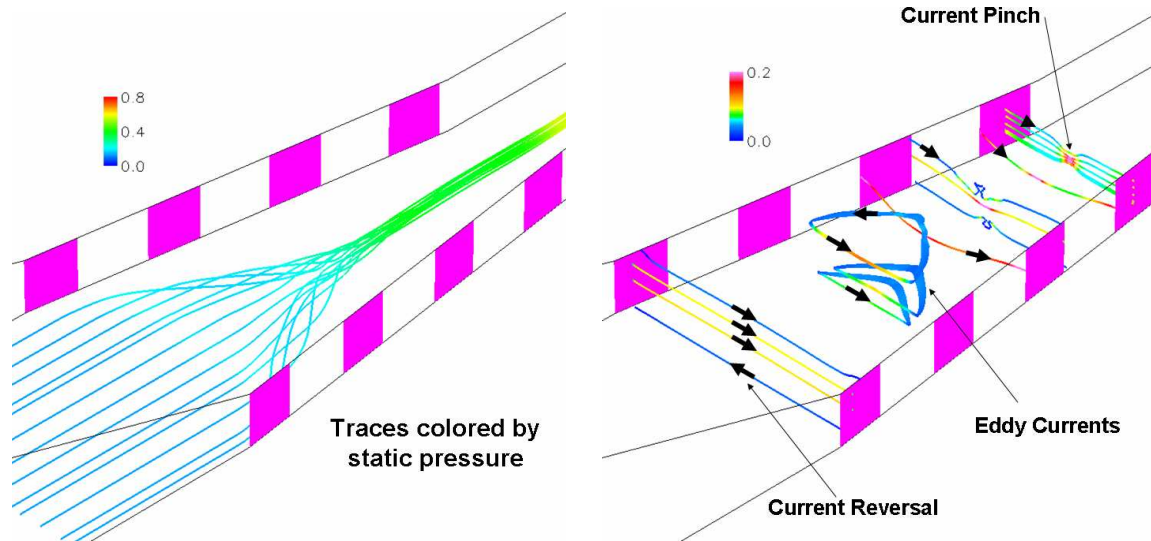
(a) Streamtrace of Vortical Structures due to Sidewall Interaction

(b) 3D-Flow Induced Effects on Current Path

Figure 1.4:   Examples of 3D MGD-Flow Interaction in AFRL Scramjet Inlet Model[21]

vertical plane. In spite of all these effects, overall MGD generation efficiently reduced inlet flow speed, indicating enthalpy was extracted, but also a net drag penalty was accrued. Conversely, the MGD accelerator operation, as configured, experienced significant heating in the boundary layer due to Joulean dissipation [11]. This loss, given by $\left|\bar{j}\right|^2/\sigma$, is an inevitable consequence of the plasma having a finite conductivity, and can be a significant concern for the weakly ionized plasmas under consideration.

1.4   Research Objective

This research task performed basic research in aeronautical sciences to support Air Force thrusts in sustained hypersonic flight and access-to-space. The main objective was to understand the fundamental capabilities of magnetogasdynamics flow field control using MGD generators and accelerators and to apply this knowledge in conjunction with AFRL towards understanding the basic phenomena occurring in MGD energy bypass design for scramjet propulsion. The information gathered will provide

insight into the development of efficient propulsion systems for sustained hypersonic flight.

1.5 Report Scope and Organization

This final report is organized into six chapters, including this introduction. Chapter II includes a presentation of the governing equations used in the computational model. The other major features of this chapter are the description of available efficiency metrics with their advantages and disadvantages and the adoption of an existing ionization model to the computational method. Electromagnetic flow control is addressed in two separate chapters. First, localized control is investigated in Chapter III with respect to mitigating flow separation within the inlet. Second, the MGD energy bypass method of improving engine efficiency and providing auxiliary electrical power is explored in IV. Finally, Chapter V summarizes the results of this research and answers the fundamental question: can electromagnetic flow control improve the performance of a flight-representative scramjet engine?

II. Governing Equations, Numerical Methods, and Performance Measures

2.1 The Magnetogasdynamic Equations

The assumptions and derivation of the governing equations of MGD flow are well-established [7, 18, 45, 49]. Their implementation in the AFRL research code used in this research has likewise been well-documented by the authors [10, 11, 13, 14]. In summary, the aerospace environment of interest for this type of problem is characterized as weakly ionized. A weakly ionized flow has a relatively low magnetic Reynolds number. Under these conditions, a relatively large magnetic field is needed to obtain a reasonable fluid-magnetic interaction parameter of order one, $Q = \sigma_0 B_0^2 L_0/(\rho_0 V_0)$. These assumptions lead to a simplified combination of the Maxwell equations for electromagnetics and the Navier-Stokes equations for fluid flow, in which the interaction between electromagnetic fields and electrically conducting gases in a continuum reduces to source terms for the Lorentz vector force $(\vec{j} \times \vec{B})$ and energy interaction term $(\vec{E} \cdot \vec{j})$ in the Navier-Stokes momentum and energy equations, respectively. The non-dimensional governing equations for the overall mass conservation, momentum conservation, and energy conservation are therefore given by Equations 2.1– 2.3, respectively.

$$\frac{\partial \rho}{\partial t} + \frac{\partial (\rho V_i)}{\partial x_i} = 0 \tag{2.1}$$

$$\frac{\partial (\rho V_i)}{\partial t} + \frac{\partial (\rho V_i V_j)}{\partial x_j} + \frac{\partial (p \delta_{ij})}{\partial x_j} - \frac{1}{Re}\frac{\partial \tau_{ij}}{\partial x_j} = Q\left(\vec{j} \times \vec{B}\right) \tag{2.2}$$

$$\frac{\partial (\rho e_t)}{\partial t} + \frac{\partial (\rho V_i h_t)}{\partial x_i} - \frac{1}{Re}\frac{\partial (\tau_{ij} V_j)}{\partial x_i} - \frac{1}{(\gamma - 1)PrM^2 Re}\frac{\partial q_i}{\partial x_i} = Q\left(\vec{E} \cdot \vec{j}\right) \tag{2.3}$$

In the above equations, ρ is the density, and p is the pressure. The velocity vector, $\vec{V}$, is composed of u, v, w components in the x, y, z directions, respectively. V_i, V_j, or V_k

also represents one of these components. τ_{ij} is the stress tensor, and q_j is the heat flux vector. $h_t = h + \frac{1}{2}V_iV_i$ is the total enthalpy, and $e_t = h_t - \frac{p}{\rho}$ is the total energy. The non-dimensional parameters are the Reynolds number Re, the interaction parameter Q, the Prandtl number Pr, and the Mach number M.

The induced magnetic field is negligible for these low magnetic Reynolds number flows. The magnetic flux $\vec{B}$ is the imposed field. Therefore, electrical current $\vec{j}$ in the source terms for the Lorentz force and energy interaction is obtained from the phenomenological form of the generalized non-dimensional Ohm's law as follows: [36]

$$\vec{j} = \sigma(\vec{E} + \vec{V} \times \vec{B}) \tag{2.4}$$

where σ is the electrical conductivity tensor calculated as products of modified Gaussians. [11]

Equations 2.1 through 2.3 can be written in flux vector form as:

$$\frac{\partial \mathbf{U}}{\partial t} + \frac{\partial \mathbf{E}}{\partial x} + \frac{\partial \mathbf{F}}{\partial y} + \frac{\partial \mathbf{G}}{\partial z} = \mathbf{S} \tag{2.5}$$

where $\mathbf{U} = \{\rho,\ \rho u,\ \rho v,\ \rho w,\ \rho e_t\}$ is the solution vector and $\mathbf{E}$, $\mathbf{F}$, $\mathbf{G}$ contain the inviscid and viscous fluxes in each direction.

and $\mathbf{S}$ is the source term:

$$\mathbf{S} = \begin{bmatrix} 0 \\ Q(j_y B_z - j_z B_y) \\ Q(j_z B_x - j_x B_z) \\ Q(j_x B_y - j_y B_x) \\ Q(E_x j_x + E_y j_y + E_z j_z) \end{bmatrix} \tag{2.6}$$

The various vectors of Eqn. 2.5 have been detailed in Refs. 14 and 12.

In order to treat physically complex domains, the governing equations are mapped to curvilinear coordinates (ξ,η,ζ)through a transformation with the following

generalized coordinates: $\tau = \tau(t)$, $\xi = \xi(x, y, z)$, $\eta = \eta(x, y, z)$, $\zeta = \zeta(x, y, z)$. The strong conservation form is employed to obtain:

$$\frac{\partial \hat{\mathbf{U}}}{\partial \tau} + \frac{\partial \hat{\mathbf{E}}}{\partial \xi} + \frac{\partial \hat{\mathbf{F}}}{\partial \eta} + \frac{\partial \hat{\mathbf{G}}}{\partial \zeta} = \hat{\mathbf{S}} \qquad (2.7)$$

with J representing the Jacobian of the transformation, $\hat{\mathbf{U}} = \mathbf{U}/J$, $\hat{\mathbf{S}} = \mathbf{S}/J$ and the contravariant fluxes:

$$\begin{aligned}
\hat{\mathbf{E}} &= \frac{1}{J}(\mathbf{E}\xi_x + \mathbf{F}\xi_y + \mathbf{G}\xi_z) \\
\hat{\mathbf{F}} &= \frac{1}{J}(\mathbf{E}\eta_x + \mathbf{F}\eta_y + \mathbf{G}\eta_z) \\
\hat{\mathbf{G}} &= \frac{1}{J}(\mathbf{E}\zeta_x + \mathbf{F}\zeta_y + \mathbf{G}\zeta_z)
\end{aligned} \qquad (2.8)$$

To simulate fine-scale turbulence, the code utilizes the popular two-equation $k-\epsilon$ model, where k is the turbulence kinetic energy and ϵ is the dissipation. New terms added to the model mimic some of the anticipated effects of the magnetic field in a simple yet effective manner. The mean flow equations were modified by replacing the molecular viscosity μ with the sum, $\mu + \mu_t$, where μ_t is the turbulent eddy viscosity and introducing the turbulent Prandtl number ($Pr_t = 0.9$) in the standard fashion [12,14].

2.2 Coupling Thermochemistry with the Magnetogasdynamic Equations

For flows with n reacting species, $n-1$ species mass conservation equations are needed to supplement the overall mass conservation equation. The species conservation equation for each species, s, is given by:

$$\frac{\partial \rho_s}{\partial t} + \frac{\partial (\rho_s V_i)}{\partial x_i} - \frac{\partial}{\partial x_i}\left(D_s \frac{\partial \rho_s}{\partial x_i}\right) - \dot{W}_s = 0 \qquad (2.9)$$

where the first two terms are the same as in the overall conservation equation, the third term represents the species diffusion (as governed by the diffusion coefficient D_s), and the final term represents the rate of species production or depletion due to chemical reaction. Because the current focus is on supersonic combustion, this code assumes the effect of species diffusion may be neglected relative to the species convection and production terms.

Across a given time step, (Eqns. 2.1– 2.3) were solved prior to the species conservation equations (Eqn. 2.9). The subsequent change in chemical composition due to the changes in the flow state and chemical reaction was then used to update the mass-averaged thermodynamic properties for the ensuing flow step. A detailed outline of the algorithm is:

1. Initialize flow variables and chemical composition at each point.

2. At each time step, solve the flow equations, assuming a constant chemical composition. The resulting mixture pressure, p, as well as the mass fluxes, ρu, ρv and ρw, will be considered invariant across the following chemistry step.

3. Calculate the mixture total enthalpy, h_t, at each point. h_t is likewise considered constant across the chemistry step. The definition of the static enthalpy is given in this context by Equation 2.10, which is the summation over all species of the heat of formation, h_s^f, and the change in enthalpy relative to standard conditions, Δh_s^{298K}, weighted by the corresponding species mass fraction, Y_s. As an aside, values of Δh_s^{298K} are determined using a temperature-based polynomial curve fit of experimental data as shown in Equation 2.11 [24].

$$h = \sum_{s=1}^{n} \left(h_s^f + \Delta h_s^{298K} \right) [Y_s] \tag{2.10}$$

$$\Delta h_s^{298K} = A_s T + \frac{B_s}{2} T^2 + \frac{C_s}{3} T^3 + \frac{D_s}{4} T^4 - \frac{E_s}{T} + F_s - H_s \tag{2.11}$$

4. Determine the change in species density due to reaction (i.e. the production source term, $\dot{W}_s$) by solving the reaction rate equations as given by Equation 2.12. Several terms in this equation require definition. First, the molecular weight of species, s, is given by MW_s. Next, $\left(v_s^{\mathcal{P}} - v_s^{\mathcal{R}}\right)_m$ is the change in stoichiometric coefficient for s and reaction, m, as the reactants, $\mathcal{R}$, are converted to products, $\mathcal{P}$. The third-body efficiency for each reaction, which is specific to the kinetics model used, is given by $\mathcal{M}_{eff,m}$. The forward rate constants, k_{f_m}, and the backward rate constants, k_{b_m}, are likewise kinetics model specific and for this research are defined by Equation 2.16 as discussed in the next paragraph. Finally, the species mole fraction is given by $[X_i]$.

$$\dot{W}_s = MW_s \sum_{m=1}^{\#Rxn} \left(v_s^{\mathcal{P}} - v_s^{\mathcal{R}}\right)_m \mathcal{M}_{eff,m} \left\{ k_{f_m} \prod_{i=1}^{n} [X_i]^{v_i^{\mathcal{R}}} - k_{b_m} \prod_{i=1}^{n} [X_i]^{v_i^{\mathcal{P}}} \right\}$$

$$(2.12)$$

5. Solve the species continuity equation, Equation 2.9, for updated values of each species density, ρ_s.

6. Use the updated values of ρ_s to get the new value for the mixture gas constant and update the mixture's heat of formation.

7. At this point, the change in temperature can be found from conservation of total enthalpy across the chemistry step as reactants, $\mathcal{R}$, are converted to products, $\mathcal{P}$. Using the assumptions from Steps 2 and 3, this conservation equation can be formulated as an implicit function of the temperature, T, as given by Equation 2.13 and solved through the application of a Newton iteration.

$$h_t^{\mathcal{R}} - h_t^{\mathcal{P}} = 0 = h_t^{\mathcal{R}} - \sum_{s=1}^{\mathcal{P}} \left(h_s^f + \Delta h_s^{298K}\right)[Y_s] - \frac{\left|\overrightarrow{V}^{\mathcal{P}}\right|^2}{2} \qquad (2.13)$$

where by Equation 2.14:

$$\left| \overrightarrow{V}^{\mathcal{P}} \right|^2 = \frac{(\rho u)^2 + (\rho v)^2 + (\rho w)^2}{\rho^2} = \left[(\rho u)^2 + (\rho v)^2 + (\rho w)^2 \right] \left(\frac{RT}{p} \right)^2 \quad (2.14)$$

8. Once the new value of T is known, a new value for mixture density, ρ is found from the perfect gas equation of state. The mass fluxes are then divided by this ρ to update the velocity components.

9. Finally, the solver returns to Step 2 and repeats the algorithm until the solution converges to steady state.

The chemistry model used for H_2–air combustion was put forth by J.S. Evans and C.J. Schexnayder, Jr. [9] and consisted of a finite rate mechanism of seven species (six reacting species and inert N_2) and eight reactions as given by Equation 2.15, where the third body, $\mathcal{M}$, varies as described in the reference.

$$H_2 + \mathcal{M} \longleftrightarrow 2H + \mathcal{M}$$
$$O_2 + \mathcal{M} \longleftrightarrow 2O + \mathcal{M}$$
$$H_2O + \mathcal{M} \longleftrightarrow OH + H + \mathcal{M}$$
$$OH + \mathcal{M} \longleftrightarrow O + H + \mathcal{M}$$
$$H_2O + O \longleftrightarrow OH + OH$$
$$H_2O + H \longleftrightarrow OH + H_2$$
$$O_2 + H \longleftrightarrow OH + O$$
$$H_2 + O \longleftrightarrow OH + H$$

$$(2.15)$$
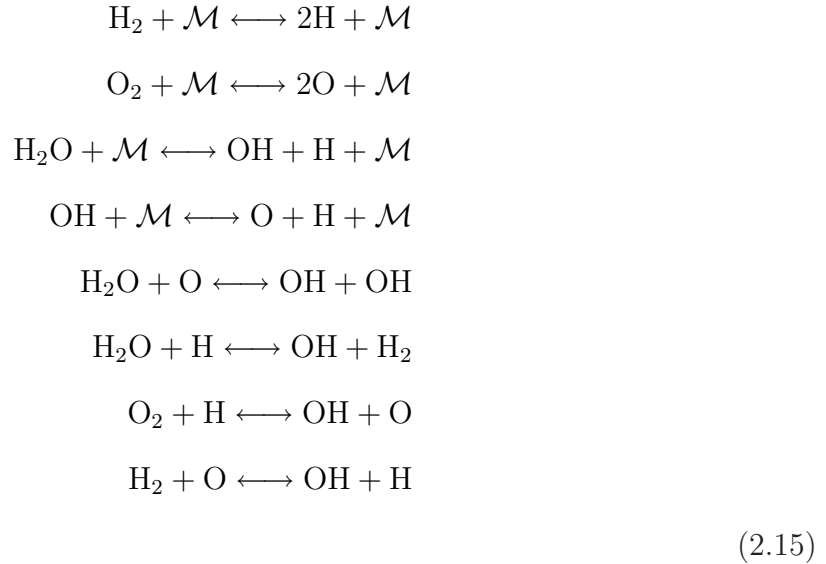
The species forward and backward reaction rate constants were determined for each reaction by an empirically-based Arrhenius rate equation as given by Equation 2.16

for the forward rate constant, k_f, and similarly for the backward rate constant, k_b, where C_{f_m}, η_m and θ_m are all curve fit constants derived from experimental data.

$$k_{f_m}(T) = C_{f_m} T^{\eta_m} e^{-\frac{\theta_m}{T}} \tag{2.16}$$

2.3   Numerical Methods

Since the influence of the magnetic and electric fields contributions are restricted to the source terms of the governing equations, conventional CFD techniques are incorporated to discretize the inviscid and viscous fluxes [12, 14]. The solver includes both the Roe flux difference and van Leer flux splitting schemes for determining the inviscid fluxes in each generalized coordinate direction. In addition, MUSCL variable extrapolation provides nominal third order spatial accuracy for the discretization. Solution monotonicity is assured with the use of a harmonic limiters. When higher accuracy is needed, a series of compact-difference methods can be incorporated. The viscous fluxes in each generalized coordinate direction can be discretized using either central differences or compact differences. For this research, the Roe flux difference scheme was used along with MUSCL variable extrapolation and the van Leer harmonic limiter for the inviscid fluxes, and the viscous fluxes were calculated using central differences.

The code includes the option of either an explicit Runge-Kutta time integration method or an implicit Beam-Warming time integration method [12, 14]. Explicit schemes severely limit the time step-size based on the size of the cells in the physical domain. To avoid this limitation, the implicit Beam-Warming method with a sub-iteration strategy is incorporated to solve the low magnetic Reynolds number form of the governing equations. The $k-\epsilon$ equations are also integrated implicitly in time but are loosely coupled to the flow equations. This loose coupling considerably reduces the expense of computing the flux Jacobians.

The MGD equations resolve the flow within the domain, but boundary conditions must be specified to define the flow conditions along the computational boundary. For these simulations, the inflow boundary incorporated a supersonic inflow boundary condition, in which all variables at inlet were set to a constant value. No-slip boundary conditions were enforced along the tunnel walls, with the wall temperature limited to a peak of 2000K. In addition, a zero normal pressure gradient was applied along the wall. Because the nominal flow was supersonic everywhere except in the small, subsonic portion of the boundary layers, the outflow boundary was set to supersonic extrapolation from the domain.

2.4 *The Control Volume Approach and Performance Analysis*

The control volume (CV) formulation of the governing equations of motion lends itself to the determination of system-level interactions and overall performance. These equations can be derived directly from the differential form of the equations by application of Reynold's transport theorem to a fixed control volume [51]. Furthermore, if the flow properties can be assumed constant across the flow cross-section, then the quasi-1D approach reduces the flow to dependence on a single spatial coordinate. Even though the inlet flow considered here has a complex 3D character, by taking area and volumetric averaging of the grid point flow properties, the quasi-1D approach can provide reasonable, conservative results. Finally, two more assumptions are made to obtain the equations that follow: (1) a single CV average value for the thermochemical properties can be taken (e.g. γ, C_V, C_p, etc) and (2) the flow is steady in the sense that the influence of any $\partial/\partial t$ terms is negligible with respect to the steady terms. With this in mind, the CV equation for mass conservation is given by Equation 2.17. Similarly, the momentum conservation equations are given by Equations 2.18– 2.20, and energy conservation is given by Equation 2.21.

$$(\rho A u)_e - (\rho A u)_i = \dot{m}_e - \dot{m}_i = \sum \dot{m}_o \qquad (2.17)$$

where the subscripts e, i, and o refer to the exit plane, inlet plane, and any mass flow through the other boundaries (e.g. cowl spillage, fuel), respectively.

$$F_x = -\dot{m}_i u_i + \dot{m}_e u_e + \sum \dot{m}_o u_o + p_e A_e - p_i A_i \qquad (2.18)$$

$$F_y = -\dot{m}_i v_i + \dot{m}_e v_e + \sum \dot{m}_o v_o \qquad (2.19)$$

$$F_z = -\dot{m}_i w_i + \dot{m}_e w_e + \sum \dot{m}_o w_o \qquad (2.20)$$

where the force components F_x, F_y, and F_z represent the total forces acting on the CV other than the inlet and exit boundaries, including those due to the Lorentz Force, if present.

$$\frac{dE}{dt} = \dot{Q}_{ht} + \dot{W}_{EM} = \dot{m}_e \left(h_e + \frac{V_e^2}{2} \right) - \dot{m}_i \left(h_i + \frac{V_i^2}{2} \right) + \sum \dot{m}_o \left(h_o + \frac{V_o^2}{2} \right) \qquad (2.21)$$

where $\dot{W}_{EM}$ is the electromagnetic interaction term, defined as the algebraic sum of the work done on the control volume by the Lorentz force and the Joulean dissipation. The final result is given by Equation 2.22. Note, that by convention, the rate of heat energy crossing the CV boundary in Equation 2.21, $\dot{Q}_{ht}$, is considered positive for heat entering the control volume.

$$\dot{W}_{EM} = \vec{E} \cdot \vec{j} = \frac{\left| \vec{j} \right|^2}{\sigma} + \vec{V} \cdot \left(\vec{j} \times \vec{B} \right) \qquad (2.22)$$

Four measures are commonly used to describe performance: the total pressure ratio, π_c, the kinetic energy efficiency, η_{KE}, the dimensionless entropy increase, $\Delta s / C_p$, and the adiabatic compression efficiency, η_c [15]. π_c and $\Delta s / C_p$ both rely on constant (or averaged) thermochemical properties to obtain analytical expressions from the solution of Gibbs' equation. Thus, while these measures by themselves will lose some accuracy for the high stagnation enthalpy flows that characterize the scram-

jet flowpath, they remain useful in determining trends when varying flow parameters. These two performance measures are given by Equations 2.23 and 2.24.

$$\pi_c = \frac{p_{t,e}}{p_{t,i}} = \frac{p_e}{p_i} \left\{ \frac{1 + \frac{\gamma-1}{2}M_e^2}{1 + \frac{\gamma-1}{2}M_i^2} \right\}^{\frac{\gamma}{\gamma-1}} \tag{2.23}$$

$$\frac{\Delta s}{C_p} = \ln\left(\frac{T_e}{T_i}\right) - \frac{\gamma-1}{\gamma}\ln\left(\frac{P_e}{P_i}\right) \tag{2.24}$$

η_{KE} and η_c are both referenced to the freestream static conditions and thus are generally preferred for this type of flow. η_{KE} (Equation 2.25) is defined as the ratio of the square of the velocity the exit flow would achieve if isentropically expanded to freestream conditions to the square of the freestream velocity. Similarly, η_c (Equation 2.26) is the ratio of the isentropic change in enthalpy to the actual change in enthalpy, when both changes are referenced to the same change in static pressure.

$$\eta_{KE} = \frac{V_e^2}{V_i^2} + \frac{2C_pT_e}{V_i^2}\left[1 - \left(\frac{p_i}{p_e}\right)^{\frac{\gamma-1}{\gamma}}\right] \tag{2.25}$$

$$\eta_c \doteq \frac{h_e - h_x}{h_e - h_i} \tag{2.26}$$

where the subscript x denotes the conditions that would exist upon an isentropic change in enthalpy across the actual static pressure change.

There is an additional performance measure commonly encountered when examining MGD flows. The enthalpy extraction/addition ratio or η_g is simply the ratio of the change in stagnation enthalpy across the MGD region to the value at the beginning of the MGD region [21, 25]. In order to obtain a simpler analytical model, total enthalpy is often assumed conserved aside from the EM-interaction due to the MGD device. However, as applied to this research, η_g includes not only the enthalpy change due to this EM-interaction but also the change due to any other effects (e.g. geometric compression, heat of combustion). Because of this it may be difficult or impossible to separate out the EM contribution, especially when multiple factors are

acting synergistically. Therefore, η_g, is best viewed relative to similar flows as done, for example, in the inlet comparisons of Chapter III.

2.5   Approximating the Non-Equilibrium Ionization with a Simplified Electron Beam Model

Freestream flight conditions of $\rho_0 = 0.01022 \text{kg/m}^3$, $V_0 = 3060 \text{m/s}$ and the leading edge width reference length of 3.602m meant that $\sigma B^2 \approx 8.684Q$ or a maximum of 43.4 for $Q = 5$. While large, these values are consistent with other proposed values [11, 30]. Figure 2.1 presents the required magnetic field for a given value of conductivity at the values of Q used. By way of comparison, the natural conductivity of air at the freestream conditions was estimated to be approximately 0.03 mho/m, implying that some form of non-equilibrium ionization is required to substantially reduce the required magnetic field.
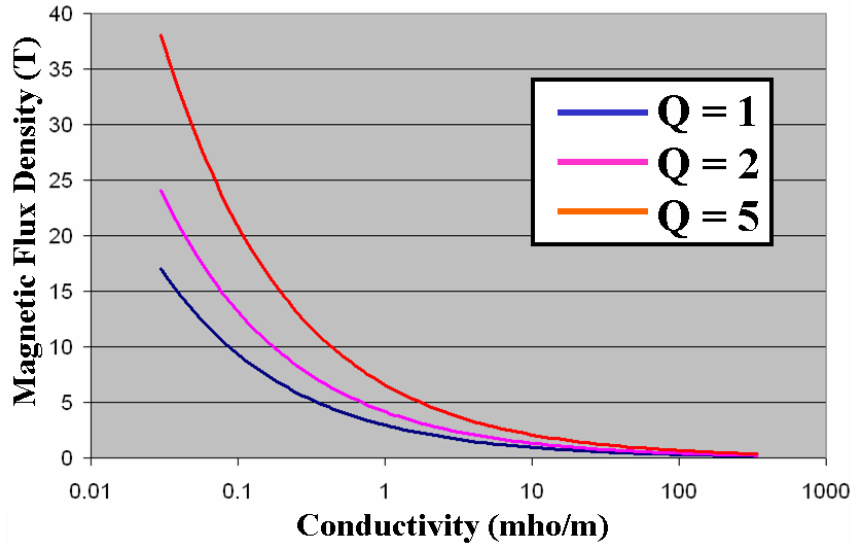
Figure 2.1:   Magnetic Field Requirements for Varying Q,σ

The computational code as currently implemented does not specify an ionization method, but rather depends on the interaction parameter, Q, and the spatial distribution of the non-dimensionalized electro-magnetic field quantities to solve the coupled equations. However, with this research, a first-order approximation of the average

magnitudes of σ_0 and B_0 is presented, as well as the required ionization power, P_{ion}, and generated electrical power, P_{gen}. To accomplish this, a model to approximate the ionization was needed that could be adapted to the results generated by the existing 3D computational code. Based on the wealth of previous work done by many in the field, it was decided the electron beam model provided a realistic approach to approximating the non-equilibrium ionization that could be readily adapted to the existing computational method. Specifically, the model of Kuranov and Sheikin [20–22] was used to determine the power spent on ionizing a unit volume of air, q_i, as given by Equation 2.27 where $j_b \approx 1.0\text{mA}$ [28] is the electron beam current, e is the electron charge, ρ is the flow density and $Y(E_b) = 7.567\text{MeV-cm}^2/\text{gm}$ is the electron stopping power as a function of the electron energy. This last quantity was taken from tabulated data for dry air with an electron energy of $E_b = 30\text{keV}$ [1].

$$q_i = (j_b/e)\,\rho Y(E_b) \tag{2.27}$$

The resulting conductivity is found from Equation 2.28 where m_e is the electron mass, $k_e = 2 \times 10^{-8}\text{cm}^3/\text{s}$ is the electron scattering constant [3], and n_e/N is an empirically-based expression for the ionization fraction as given by Equation 2.29 [22]. The number density, N, can be related to the density by $N = \left(\frac{RN_A}{R_u}\right)\rho$ where R is the specific gas constant, R_u is the universal gas constant, and N_A is Avogadro's number.

$$\sigma = \frac{e^2}{m_e k_e}\left(\frac{n_e}{N}\right) \tag{2.28}$$

$$\frac{n_e}{N} = 1.17 \times 10^{-5} \cdot \left(10^{34}\frac{q_i}{N^2}\right)^{0.6} \tag{2.29}$$

Having a value of q_i and σ at each point, it is a simple matter to integrate over the plasma volume defined by the modified Gaussian [11] to arrive at the total power required for ionization, P_{ion}, and an overall mean value for σ_0. Then Equation 2.30 is used to obtain a corresponding value for the mean magnetic flux density where the asterisked quantities are the non-dimensional values produced by the computa-

tional code. In a similar manner, the electrical power generated is simply found by integrating Equation 2.31 over the plasma volume.

$$(\sigma B^2)_0 = \left(\sigma^* B^{*^2}\right) \left(\frac{\rho V}{L}\right)_0 Q \qquad (2.30)$$

$$P_{gen} = \int \int \int \left(\overline{j} \cdot \overline{E}\right) d\,(Vol) \qquad (2.31)$$

III. Localized Electromagnetic Flow Control

3.1 The Baseline Engine Inlet

A wide assortment of techniques was implemented to create the inlet geometry shown in Fig. 3.1 [23]. The external-internal compression inlet performed marginally well insofar as it increased the mean static pressure to $57P_0$ at the inlet throat while limiting the static temperature rise to $5.1T_0$ as seen in Fig. 3.2(b). (Reference pressure and temperature were $P_0 = 684Pa$ and $T_0 = 233K$). However, this result was 23% below the minimum desired combustor inlet pressures of 1/2atm, an outcome directly attributable to the inability of the quasi-1D, inviscid inlet analysis to account for the three-dimensional effects discussed in this section. A review of Fig. 3.2(b) reveals that the local cross-sectional average of Mach number decreased fairly uniformly through the inlet from the reference value of $M_0=10$ to an inlet throat value of M=3.81. This value at the throat is still higher than the Mach 1–3 range desired for a scramjet combustor, providing an opportunity for improvement through the use of MGD interaction. In addition, Fig. 3.2(b) shows the axial velocity experienced a substantial decrease in the vicinity of a large separation region downstream of the cowl shoulder. This separation region, which also caused the localized temperature spike at x=17.25m in Fig. 3.2(a), is discussed in greater detail below. It was also a contributing factor to the baseline heat transfer of 69.6MW out of the inlet walls. Regarding overall inlet performance and efficiency, a force balance using Equations 2.18 – 2.20 revealed a baseline drag of 86kN, lift of -67kN, and yaw of 870N. The negative lift, or down force, was due to a mass flow spillage at the cowl lip which is described in the following paragraph. Because the computational domain did not model the external flow around the cowl, it is not certain how much this down force would contribute to the overall vehicle flow field and force balance. Finally, the system efficiencies were given by: $\pi_c = 0.1519$, $\eta_{KE} = 0.8868$, $\Delta s/C_p = 0.4827$, and $\eta_c = 0.7525$, as defined by Equations 2.23– 2.26, respectively. The last result showed the inlet performed somewhat less efficiently than the nominal value of $\eta_c = 0.9$ used by Heiser and Pratt in their analysis [15]; a fact that was attributable to three key inlet flow features.
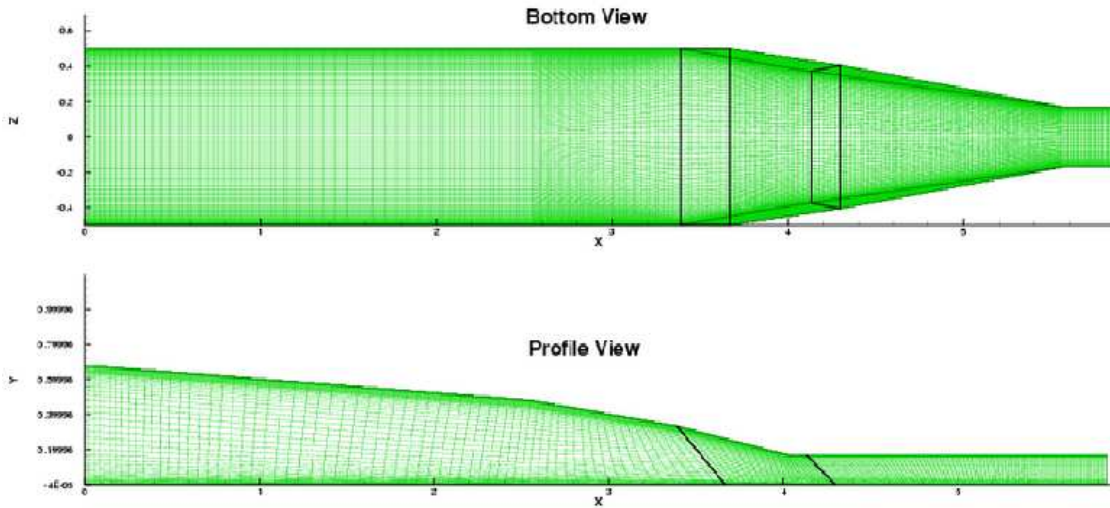
Figure 3.1:   Inlet Grid Normalized by Freestream Air Capture Width of 3.6m
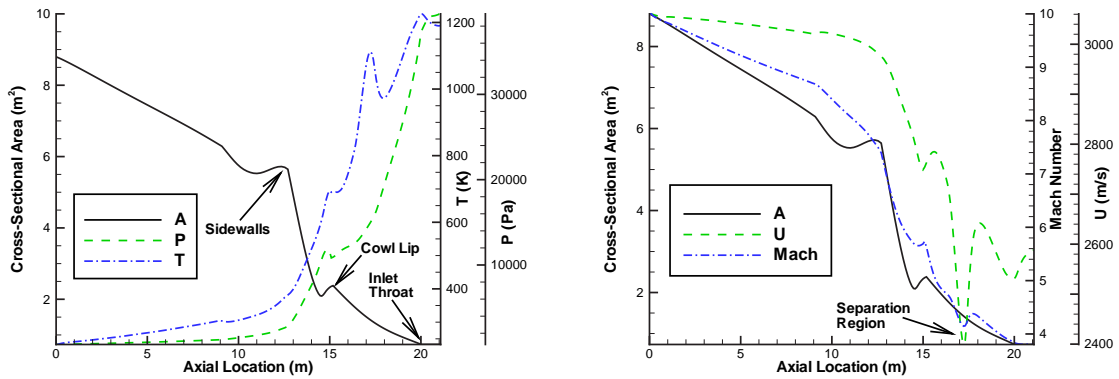
(a) Mean Values of Static Pressure and Temperature within Baseline Inlet

(b) Mean Values of Mach Number and Normalized Axial Velocity within Baseline Inlet

Figure 3.2:   Baseline Mach 10 Inlet Geometry and Selected Flow Properties

3-2

First and foremost, 59 kg/s, or roughly 22%, of the freestream mass flow spilled at the bottom cowl lip, never entering the internal compression portion of the inlet. This spillage loss was a purely 3D effect attributable to the sidewall interaction. The additional sidewall compression caused the flow to seek pressure relief by turning downward, an effect previously documented by Holland [16, 17]. This effect was clearly visible in Fig. 3.3(a) by the sharp decrease in mass flow rate at the cowl lip and in Fig. 3.3(b) by the increase in a negative v-velocity component near the cowl. Normally, this spillage could be countered by moving the cowl lip forward, however, the pressure relief is a desired effect for engine starting which would occur at lower Mach numbers and higher pressures. Therefore, although it was not needed for the cruise test conditions examined in this research, this geometric feature was kept to improve the realism of the overall design.
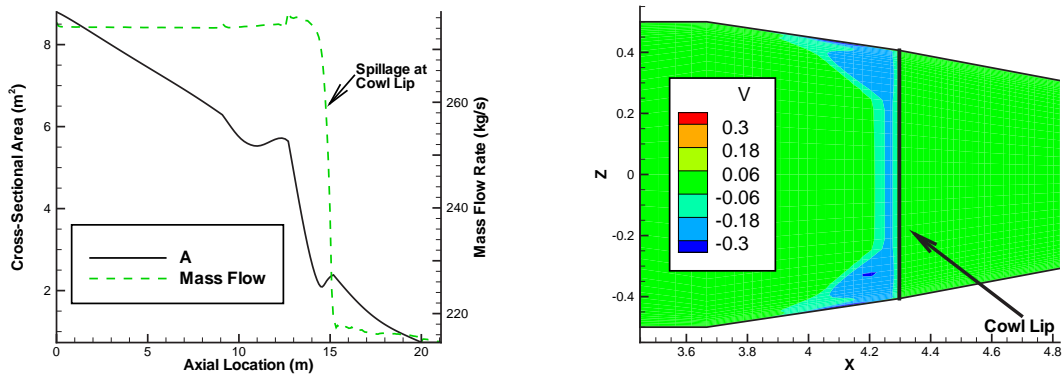
(a) Mass Flow Rate

(b) Normalized v-Velocity Contours Demonstrating Mass Spillage in Cowl Lip Vicinity

Figure 3.3:   Baseline Inlet Mass Flow Emphasizing Cowl Spillage

Second, large areas of expanded flow developed downstream of the inlet shoulder (opposite of the cowl lip on the body side) and at the inlet throat. These expansions are clearly visible in Fig. 3.4(a) as the blue shaded, low pressure regions. Note, the pressure contours in this figure have been normalized by $P_0 = 684$Pa. The pitch plane expansion at the cowl shoulder was particularly detrimental to the compression

(a) Pressure Contours Normalized by $P_0 = 684$Pa

(b) U-Velocity Contours Normalized by $V_0 = 3060$m/s
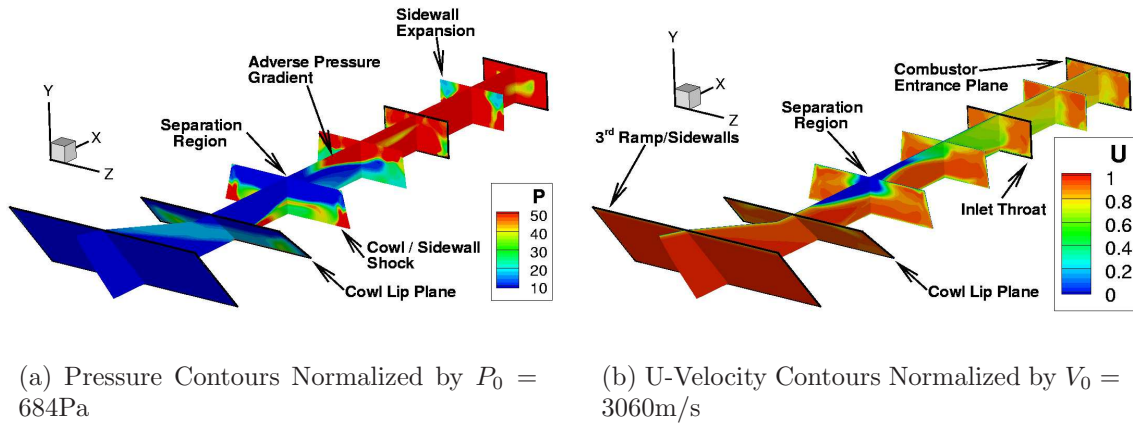
Figure 3.4:   Baseline Inlet Flow Emphasizing Critical Flow Features

efficiency as a large region of the body-side flow returned to nearly freestream pressure conditions just prior to interacting with the shock reflected from the cowl lip. This interaction created a separation zone as shown in Fig. 3.4(b), fairly symmetric about the k-midplane, due to the severe adverse pressure gradient formed where the cowl lip shock reflected off of the body side and was met by the low pressure, high velocity expanded flow around the shoulder. The high pressure tended to reverse the flow in the vicinity of the boundary layer and propagate the pressure gradient upstream of the actual shock impingement until equilibrium was reached. This expansion-separation caused an estimated loss of nearly 10kPa in the mean pressure at the inlet throat ($x \sim 20$m in Fig. 3.2) and a significant amount of heating due to the locally stagnating flow, as seen in the temperature contours of Fig. 3.5. A further sidewall expansion into the isolator resulted in an additional 3kPa mean pressure loss.

Finally, vortical structures, similar to the ones reported by Gaitonde [11], were observed from just downstream of the third pitch-plane ramp (Fig. 3.6(a)) through the rest of the inlet (Fig. 3.6(b)). These vortices, were due primarily to the 3D, viscous interaction brought about by the corner flows. This feature was enhanced by the sidewall compression shocks intersecting with those due to the pitch-plane
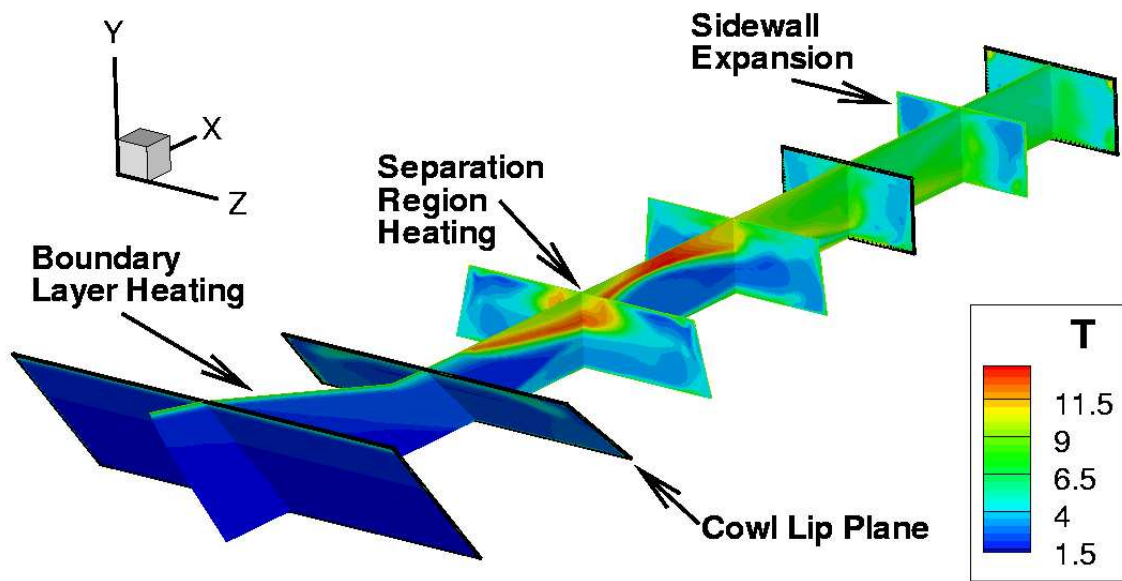
Figure 3.5:   Temperature Contours in Baseline Inlet Normalized by $T_0 = 233K$
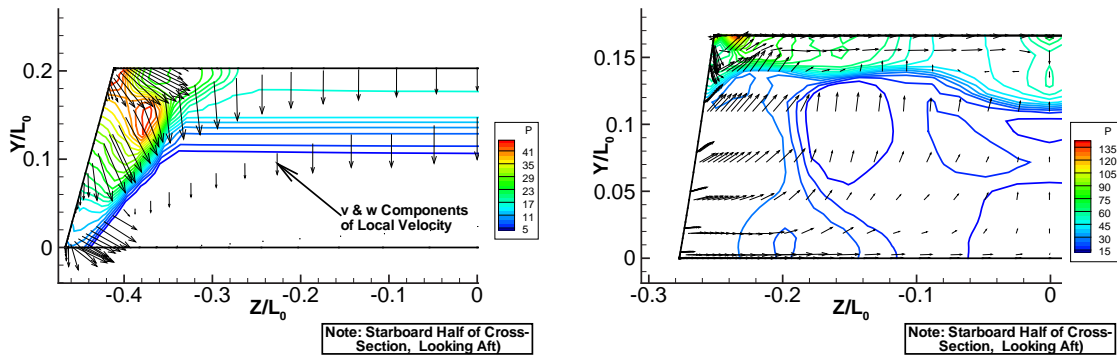
(a) Between 3rd Pitch Ramp and Cowl Plane, x=14.0m

(b) Midway Between Cowl and Throat, x=18.0m

Figure 3.6:   Selected Cross-Sections of Baseline Inlet with Pressure Contours Normalized by $P_0 = 684Pa$ and Velocity Vectors that Demonstrate Presence of 3D Vortical Flow Structures

compression. The net effect was an increase in the inlet total pressure loss and entropy rise and a decrease in overall flow momentum and compression efficiency.

3.2 Overview of the MGD Parameter Study

We raise the question as to whether MGD can be applied in this situation to mitigate or prevent the formation of the separation zone, improving the overall inlet flow field and specifically the flow entering the combustor. Two concepts were considered. The first concept utilized an MGD generator to increase pressure, especially in the cowl shoulder region, to better match that of the reflected shock. Alternatively, an MGD accelerator was considered to increase flow momentum in the portions of the inlet subject to locally expanding flow. This was hypothesized to be especially helpful when focused on the low momentum boundary layer where the adverse pressure gradient initiated flow separation.

Thirty-two different cases of localized EM fields and corresponding regions of specified conductivity were applied immediately downstream of the cowl shoulder on the body side in an effort to mitigate this performance loss. In all cases, the $\vec{B}$ field was uniform and aligned in the $+Y$ direction, and the $\vec{E}$ field was likewise uniform but aligned in the $-Z$ direction. Four different distributions for σ were explored; the two primary cases, referred to as Case 1 and Case 2, respectively, appear as the contoured regions in Fig. 3.7(a) and 3.7(b) . These two cases differed only in the axial extent of the plasma volume. For both cases, an additional subcase was explored wherein the conductivity was centered just outside the boundary layer as in Fig. 3.7(c). This subcase simulated an electron beam with the maximum conductivity centered several centimeters from the wall. The conduction current density, $\vec{j}$, was given by Ohm's Law in Eqn. 2.4 and was therefore in the $\pm Z$ direction depending on the magnitude of the non-dimensional load factor, k, which was tested at values of 0.0, 0.7, 1.0, and 1.3. The Lorentz force as given by $\vec{j} \times \vec{B}$ was then in the $-X$ direction (or decelerating the flow) for $k < 1$ and in the $+X$ direction (accelerating)

(a) Case 1
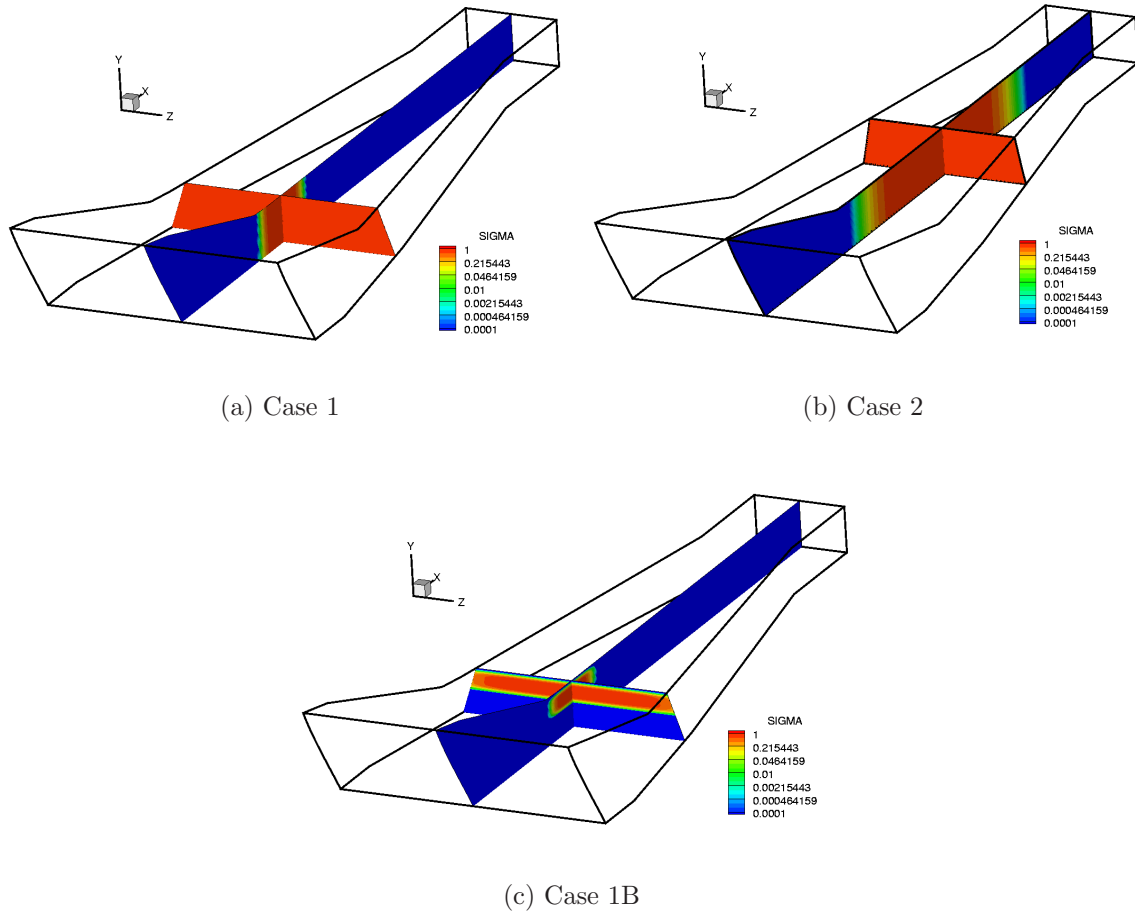
(b) Case 2

(c) Case 1B

Figure 3.7:   Full Cross-section Non-Dimensional Conductivity (SIGMA) Profiles in Inlet
(a) Case 1: Conductive region is limited to upstream of separation region.
(b) Case 2: Conductive region extends from cowl lip to inlet throat.
(c) Case 1B: Conductive region centered outside of boundary layer.

for $k > 1$. Finally, interaction parameters of $Q = 1$ and 5 were examined at the prescribed freestream flight conditions in order to gauge the effect of increasing $\vec{B}$.

3.3   Results from Conductivity Case 1

The addition of EM fields had limited effect on the outflow properties, with the exception of the $k = 0$ parameter cases, that resulted in extreme dissipative heating. This heating increased average temperatures 24% and 77% above baseline for $Q = 1$ and $Q = 5$, respectively. This was due to the fact that, with no external

load applied, all of the extracted electrical energy must dissipate within the flow itself. The accelerator case, $k = 1.3, Q = 5$, also experienced additional heating, but to a lesser extent, due to the deposition of additional external energy. For this case, the $Q = 5$ interaction elevated the temperature 18% above baseline. For the remaining parameters, Mach number, γ, and temperature were virtually unchanged from the baseline case. The pressure showed the same trends as temperature but to a lesser degree. For $k = 0$, pressures increased above baseline by 12% and 54%, and for $k = 1.3$, $Q = 5$, the pressure increase was 16%. As Fig. 3.8 shows, only the $k = 0.0, Q = 5$ case exhibited substantial gains in pressure upstream of the inlet throat, due to the EM interaction upstream of the separation region. The expansion at the inlet throat, however, had a dominant influence on the flow, drastically reducing any potential pressure increases.

With the exception of $k = 0$ and $k = 1.3, Q = 5$, the efficiencies for Cases 1 and 1B were only marginally impacted as seen in Fig. 3.9. (Note: in these comparison bar charts to follow, the numbers 1, 1B, etc. refer to the conductivity profile, while "kX.X" refers to the load factor and Q the interaction parameter used.) The greatest impact on efficiency was with $k = 0, Q = 5$, where π_c was reduced to 3% of the freestream value and η_C decreased by 6.7% with respect to baseline. $\Delta s/C_p$ and η_{KE} were similarly impacted with an increase of 49% and decrease of 4%, respectively, for this case. In an interesting result, it was noted that the largest increase in η_{KE}, 8% above baseline, occurred for $k = 1.3, Q = 5$. This makes sense from the perspective that energy external to the inlet was added in a manner that increased the kinetic energy and thus the momentum in the inlet, as desired.

Following the same trend discussed above, Fig. 3.10 reveals that the parameter $k = 0, Q = 5$ had the greatest impact on drag at 158% greater than baseline, corresponding to the highest Lorentz force at -111.0kN. For constant k, higher Q meant higher Lorentz force as expected. Also, as one would expect, increasing the departure from $k = 1$ increased the Lorentz force. This was readily apparent in the overall axial force imposed on the inlet. At $k = 1$, the interaction was minimal and the net drag
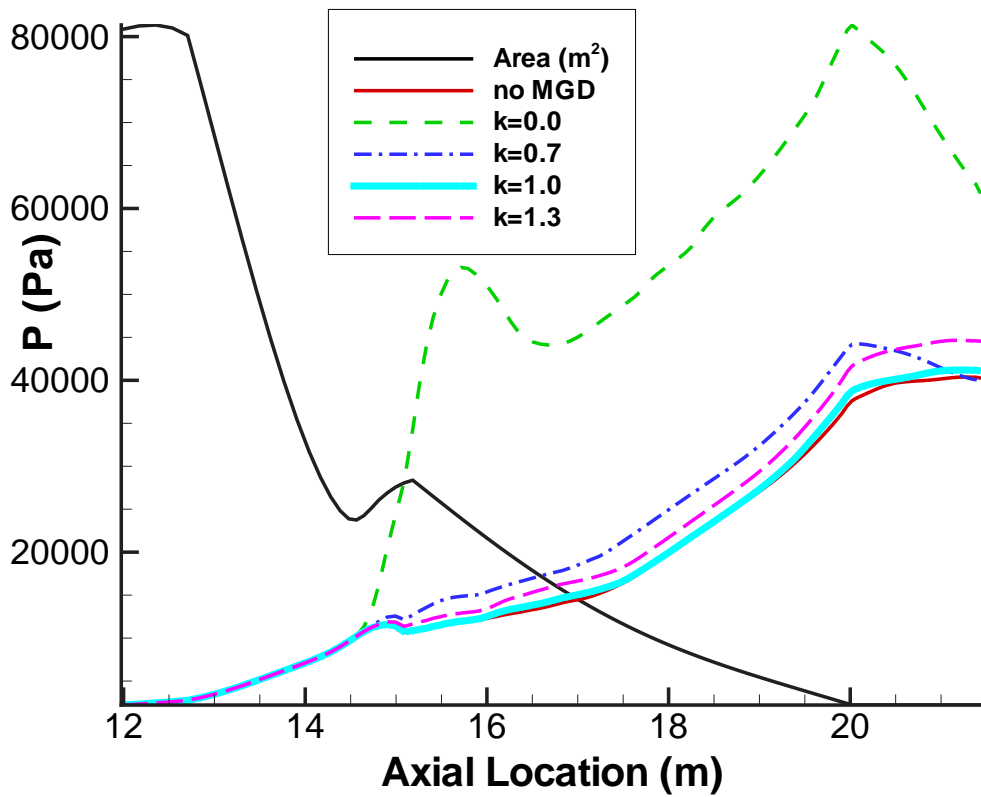
Figure 3.8: Mean Inlet Pressure for Case 1 with Varying k and $Q = 5$
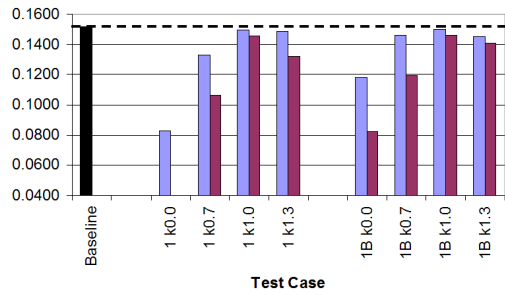
(a) Total Pressure Ratio
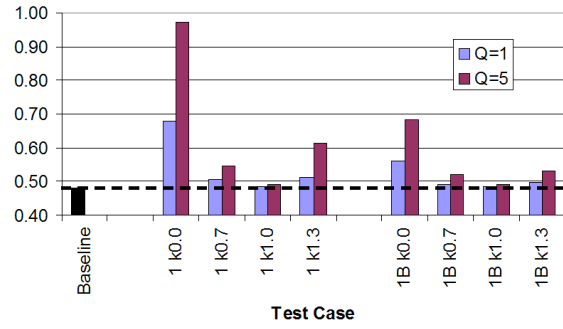
(b) Dimensionless Entropy Rise
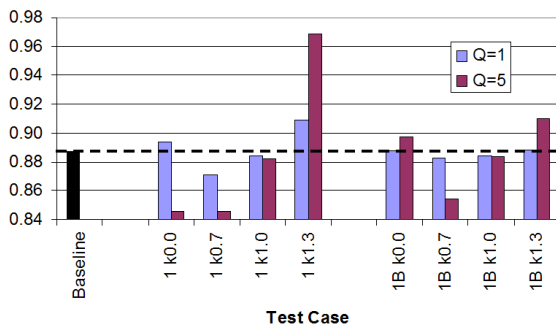
(c) KE Efficiency

(d) Adiabatic Compression Efficiency

Figure 3.9:   Inlet Efficiency Metrics for Cases 1 and 1B
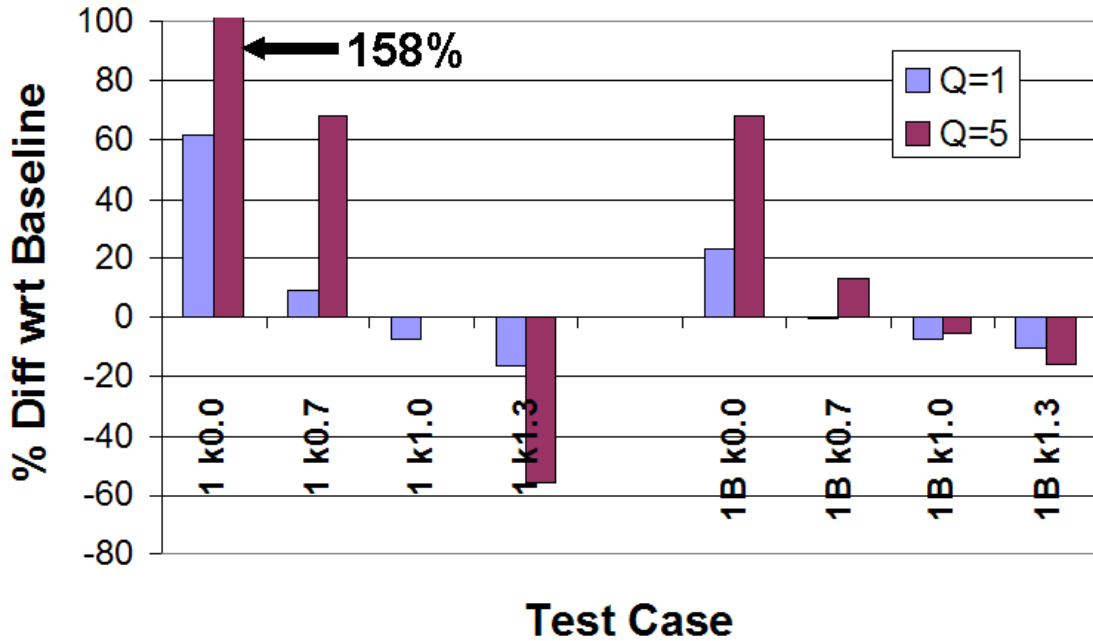
Figure 3.10:   Comparison of Net Inlet Drag for Conductivity Case 1

was actually reduced 7% below baseline. The biggest decrease in drag occurred, as expected, for $k = 1.3$, where the positive Lorentz force for $Q = 1$ was 10kN and for $Q = 5$ was a 42kN. This resulted in drag reductions of 16% and 56%, respectively, with respect to baseline. In an unexpected result, it was observed that as k went to zero there was a significant increase in mass flow spillage out of the inlet at the cowl lip. This was unique to Case 1 and was due to the full cross-section conductivity profile that extended upstream of the cowl lip plane. In effect, the Lorentz force allowed the bypass of an additional 18kg/s of air around the cowl. This additional mass flow slightly mitigated the drag increase induced by the Lorentz force. In effect, this produced a thrust, just as it would in a bypass turbofan engine. This additional spillage was easily visualized by comparing the increased thickness of the spillage contours for the $k = 0, Q = 5$ parameters as seen in Fig. 3.11 to those of the inlet without MGD as seen in Fig. 3.3(b).

As discussed previously, the time rate of energy change in the control volume, dE/dt, is equal to the heat transfer rate through the control volume (CV), $\dot{Q}_{ht}$, plus
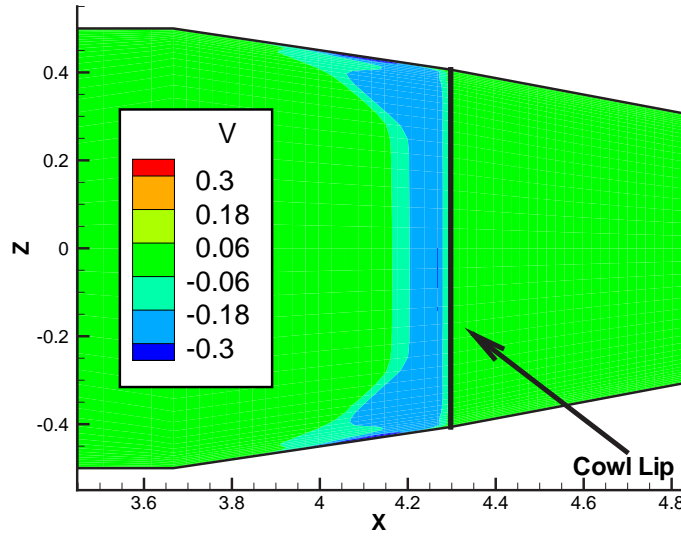
Figure 3.11: v/V_0 Contours Demonstrating Additional Cowl Lip Mass Spillage for $k = 0.0$, $Q = 5$

the EM energy interaction, $\dot{W}_{EM} = \vec{E} \cdot \vec{j}$. All of the EM cases deposit some energy into the flow through dissipation, with the amount increasing as k departs from a value of 1. Interestingly, while all cases had a net heat transfer out of the CV, some of the MGD cases exhibited less overall heat transfer than the baseline case. With the exception of $k = 0$, all of the $Q = 1$ cases had 5%–17% less as seen in Fig. 3.12. These decreases were attributed to the fact that the stagnation region due to separated flow moved slightly farther away from the wall, while at the same time the low interaction of $Q = 1$ contributed only 25%–30% of its $Q = 5$ amount. A close-up examination of the separation region revealed this unexpected result; a result that would later become more significant in plasmas limited to the near wall region. From Fig. 3.13(a) and (b) it was evident the EM cases caused the separation region to actually grow compared to the baseline case. However, this same effect caused the stagnant flow to also move away from the wall, creating a buffer zone of relatively lower temperatures next to the wall as seen in Fig. 3.13(c) and (d). This change in the heat distribution decreased the wall heat transfer by a small amount.
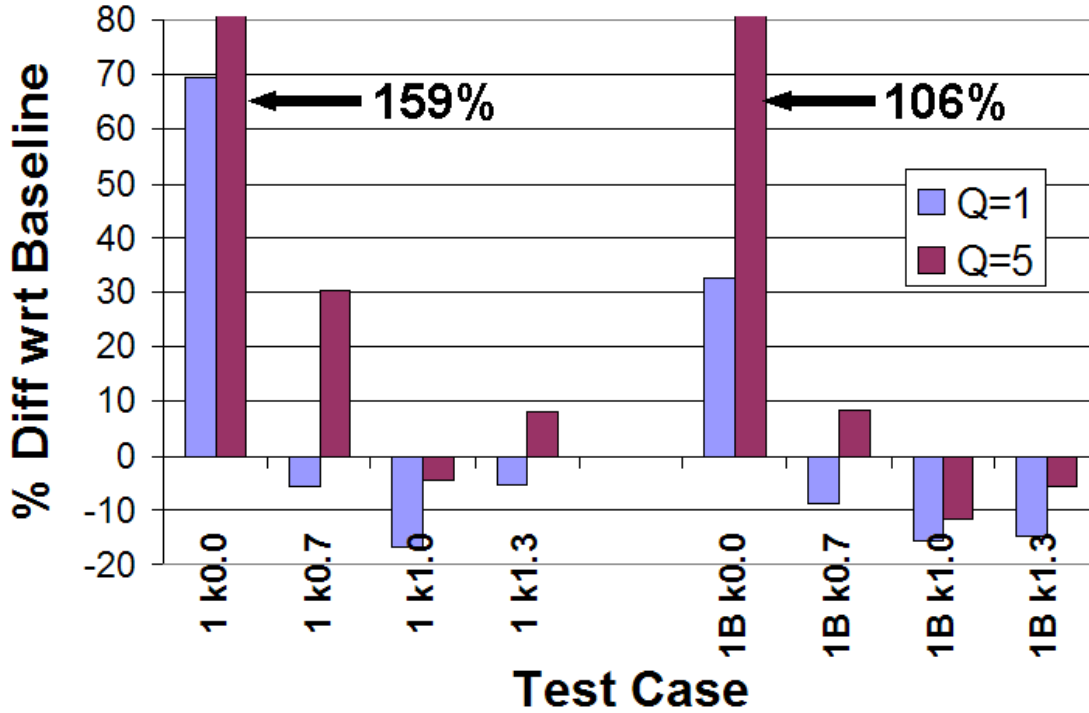
Figure 3.12: Comparison of Normalized Heat Transfer for Conductivity Cases 1 and 1B

Conversely, the maximum value of 180MW (or 159% above baseline) occurred for $k = 0, Q = 5$. $k = 0.7$ and 1.3 cases inject roughly the same amount of dissipation into the flow on the order of 9 and 34MW for $Q = 1$ and 5, respectively. However, whereas dissipation constituted roughly 40% of the total $\dot{W}_{EM}$ for $k = 0.7$, it comprised only 27% of the total for $k = 1.3$. Therefore, as an overall measure, the generator case at $Q = 5$ reflected an overall greater heat transfer rate through the CV boundaries. The $k = 1$ cases put the least amount of dissipation into the system (on the order of 1.2MW–3.6MW) because $k = 1$ represents the open circuit case where the conduction current is approximately zero. Joulean dissipation varies directly with the current, thus the lower the current (i.e. k closer to 1) the less the flow is heated.

Regarding the ionization model, the conductivity region filled approximately 3.0m³ with values of σ ranging between 0.63 and 0.86 mho/m. B-fields were on the order of 3.3T for $Q = 1$ and 7-8T for $Q = 5$. Net power generation was simply the difference between the generated electric power, P_{gen}, and the ionization power,
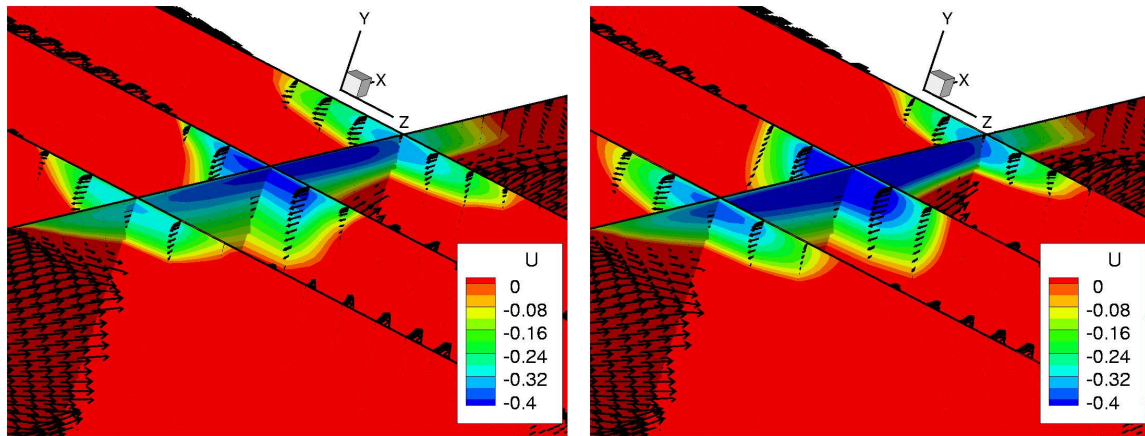
(a) Baseline u/V_0 Contours

(b) Case1, k=0.7, Q=1 u/V_0 Contours
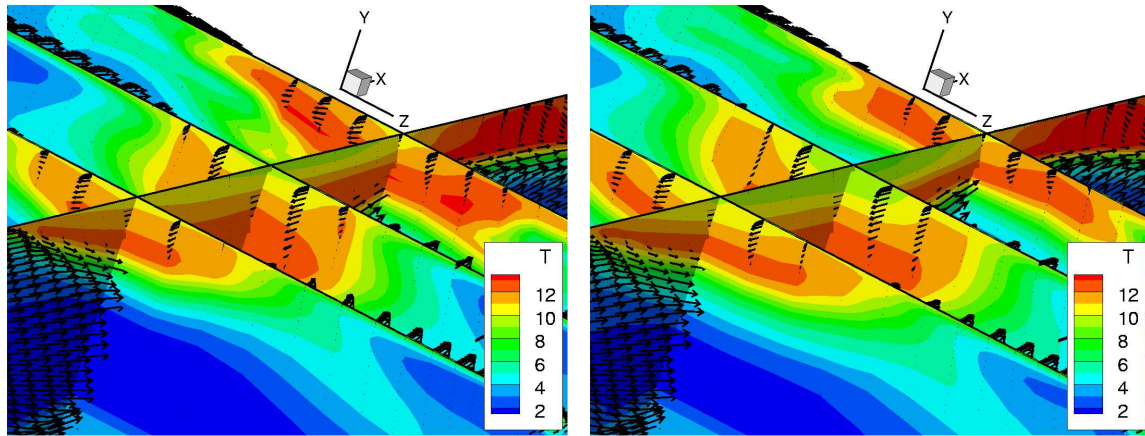
(c) Baseline T/T_0 Contours

(d) Case1, k=0.7, Q=1 T/T_0 Contours

Figure 3.13: Impact of EM Interaction on Inlet Separation Region where Arrows Represent the Normalized Local Velocity Vector

P_{ion}. Referring to Fig. 3.14, only the $k = 0.7$ cases demonstrated a meaningful net power generation with 18MW for $Q = 1$ and 82MW for $Q = 5$. The required power for ionization was on the order of 1.3–1.5MW for all cases. The enthalpy extraction ratio, η_g, was typically in the range of 10% - 20% but reached a maximum of 31% for the $k = 0.0$, $Q = 5$ generator as shown in Fig. 3.15. The $k = 1.3$, $Q = 5$ accelerator actually increased the enthalpy by 1%. However, that this measure includes changes due to both EM-interaction as well as geometric compression.
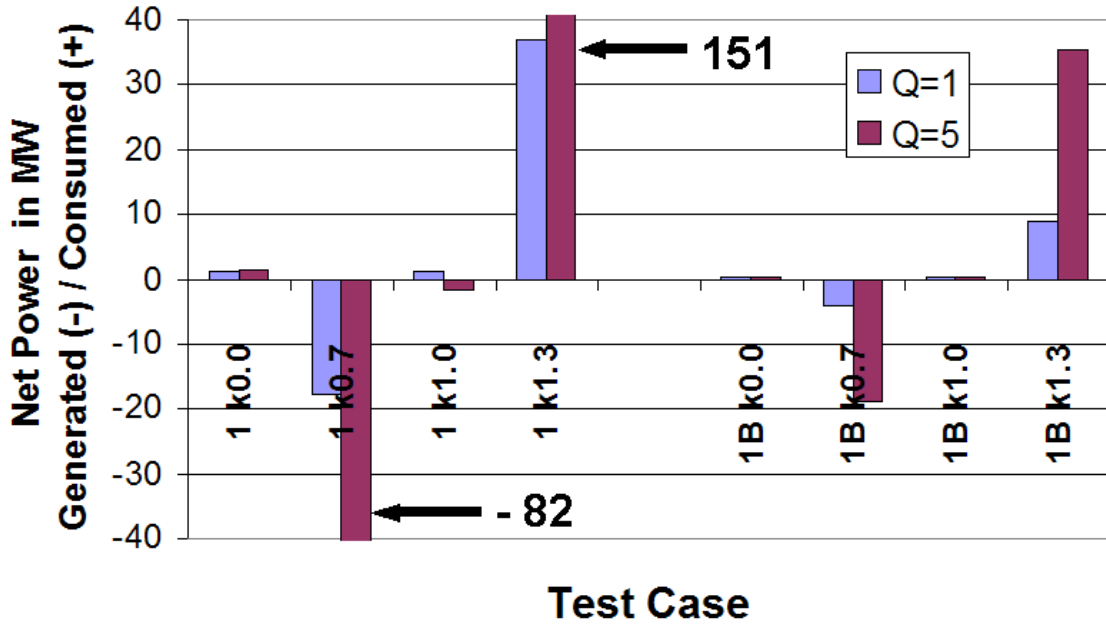
Figure 3.14:   Comparison of Net Electric Power Generated/Required for Conductivity Cases 1 and 1B

3.4   Results from Conductivity Case 1B

In contrast to Case 1, we limited the conductivity for this case to the near-wall region of the cowl shoulder. Case 1B, with a plasma volume of 1.44m^3, more accurately simulated an electron beam ionization source with the maximum conductivity centered several centimeters from the wall and then falling off rapidly in the direction normal to the wall. As in Case 1, the addition of EM fields had a small, but noticeable, effect on the outflow properties, primarily with respect to temperature
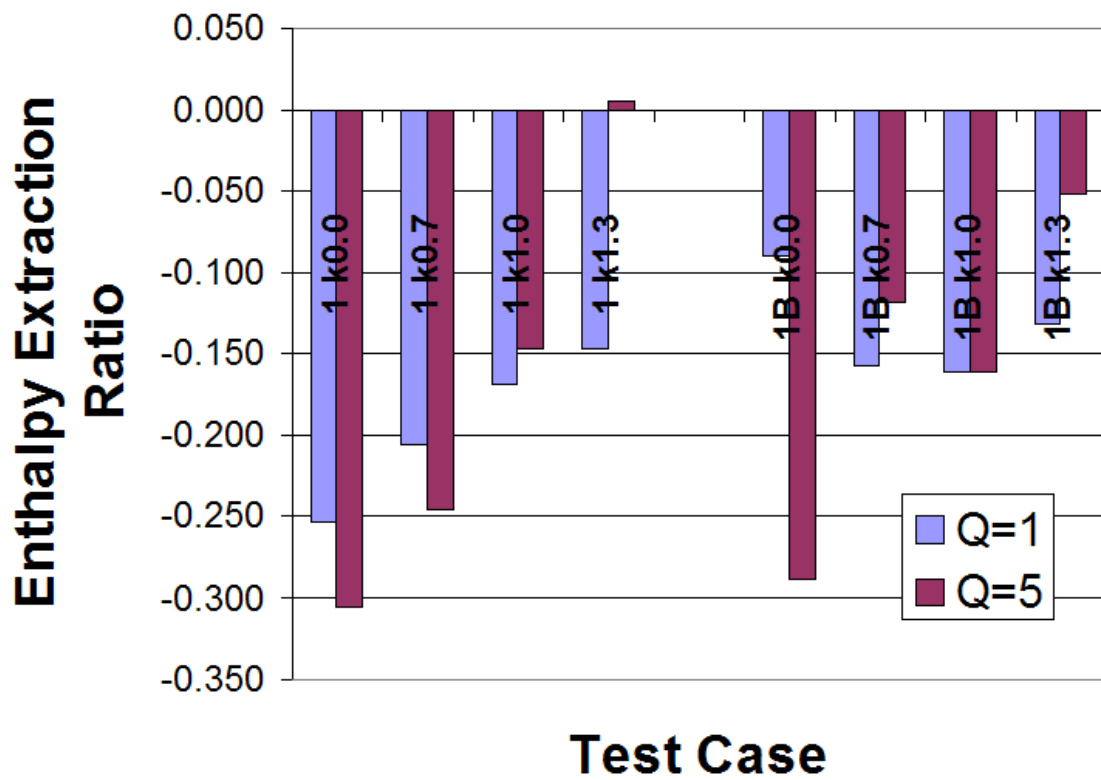
Figure 3.15: Comparison of Enthalpy Extraction/Addition for Conductivity Cases 1 and 1B

and pressure increases. However, the magnitude of these changes was much less than for the same EM interaction applied to Case 1. For example, the greatest change in exit pressure occurred for $k = 0.7, Q = 5$ and amounted to a 6.7% increase above the baseline inlet. This was expected, in light of Case 1, as the interaction region for 1B was only 48% of Case1. However, forces, heat transfer and EM terms did vary for differing parameters as applied to Case 1B, as discussed below.

Referring back to Fig. 3.10, drag varied from 16% less than baseline for the $Q = 5$ accelerator to 68% more than baseline for the $k = 0.0, Q = 5$ parameters. Overall, these numbers reflect the same trends as in Case 1 but typically at magnitudes of 1/3 to 2/3 of their Case 1 counterparts. As with Case 1, for a given k, there was an obvious change in drag for increased Q, due to the increasing magnitude of the Lorentz force. The near-wall conductivity region (being limited to the opposite side of the flow field away from the cowl lip) did not induce any additional mass spillage. Therefore, there was no contribution to thrust due to bypassed air flow as seen in Case 1. Regarding heating, all of the EM cases deposited energy into the flow through dissipation, but typically in less amounts than for Case 1. The heat transfer rates out of the control volume reflect this (Fig. 3.12). For Case 1B, the minimum and maximum values for the heating, $\dot{Q}_{ht}$, were 59MW and 143MW. The same trends as for Case 1 were seen in that $k = 0$ by far produced the most Joulean dissipation, $k = 1.3$ and $k = 0.7$ were comparable, and $k = 1.0$ produced the least amount. It was interesting to note that at $Q = 1$ Cases 1 and 1B had very similar values of wall heating for corresponding k values (with the exception of the $k = 0$ parameter). This fact demonstrated that the placement of EM-interaction near the wall was the driving factor in determining the wall heat transfer. Overall, the targeted application of conductivity appeared to be a relatively efficient method of limiting the overall drag increase due to Lorentz force. However, further work is recommended in order to determine the optimum distance off the wall to target the electron beam ionization in order to minimizing the additional wall heat load while retaining the drag reduction benefit.

Conductivity for these cases was somewhat higher than in Case 1, ranging between 0.85 and 0.97 mho/m. This was because densities near the wall were less than in the core flow, which from Equations 2.27– 2.29 implied conductivity should be higher as $\sigma \propto 1/\sqrt{\rho}$. By the same reasoning, the required P_{ion} per unit volume was also less than for Case 1. Magnetic fields were on the order of 3T for $Q = 1$ and 6.5-7T for $Q = 5$. Once again, as seen in Fig. 3.14, only the $k = 0.7$ MGD generator cases demonstrated a substantial net power generation after ionization. A net of 4.1MW was produced for $Q = 1$ and 19MW for $Q = 5$ which was 23% of that produced for the corresponding parameters applied to Case 1. The required power for ionization was on the order of 0.5MW for all cases. The enthalpy extraction ratios, η_g, were generally comparable to Case 1, which in light of the differing volumes of the interaction region, reveals that the effect of enthalpy extraction due to EM interaction is not as significant as other mechanisms such as wall heat transfer.

3.5   *Summary of Conductivity Cases 1 and 1B*

From this analysis, it appeared that neither of the control mechanisms presented in Case 1 nor 1B were effective at significantly increasing the mean pressure at the outflow plane or improving efficiency. One exception to this conclusion regarding pressure for $k = 0.0, Q = 5$ must be made. However, even in this case the quasi-1D plot of Fig. 3.8 revealed that any gains incurred from the EM interaction upstream of the separation region were substantially reduced by the sidewall expansion into the isolator at the inlet throat. Several notable improvements were observed, though. Placement of the EM-interaction region near the wall was the most important factor in determining the wall heat transfer, and targeting the conductivity to this region did appear to be a relatively efficient method of limiting drag increases. However, these two conclusions together mean further work is needed in order to determine the optimum distance off the wall to target the electron beam ionization. Finally, the additional mass flow spillage caused by placing the interaction region near the cowl lip had a noticeable impact on the inlet flow. While developing a mass flow rate

active control system along the lines of Macheret's conceptual work [30], was beyond the scope of this work, this computational modelling serves as the first high fidelity proof of this potential application.

3.6   *Results from Conductivity Case 2*

Case 2 continued the conductivity region downstream through the separation region until reaching the inlet throat as shown in Fig. 3.7(b). This plasma was about 2.6 times the volume of the Case 1 plasma, or 7.59m^3. Consequently, the impact to forces, heat transfer and, in contrast to Case 1, exit plane flow properties was significant and varied greatly with the different parameters. For example, as shown by Fig. 3.16 the exit plane pressure was 30kPa, or 74%, above the baseline case for $k = 0.0, Q = 5$. Other than the $k = 0.0$ parameter, $k = 0.7$ cases showed appreciable pressure increases of 18% and 25% for $Q = 1$ and 5, respectively. However, all of these pressure rises were accompanied by a large amount of dissipative heating, resulting in a maximum mean temperature of 3265K for the $k = 0, Q = 5$ case. It was apparent from these results and a review of Fig. 3.8 and Fig. 3.16 that raising the pressure in the isolator was accomplished most effectively by modifying the sidewall expansion fans into the inlet throat.

Looking further at the drag forces and heating, the accelerator parameters of $k = 1.3, Q = 5$ reduced the net inlet drag to 16kN (or 81% less than baseline), as shown in Fig. 3.17, but at the substantial cost of 240MW of electrical power put into the system. While all cases resulted in overall inlet drag, the $k = 1.3, Q = 1$ case likewise reduced the baseline value by 31%, at a cost of only 30% of the electrical power consumed at $Q = 5$. As k decreased (or Q increased for a given k), the drag increased, reaching a maximum value of -404kN (a 368% increase with respect to baseline) for $k = 0, Q = 5$. This made sense in both respects as a decreasing k and/or increasing Q means an increasing Lorentz force in the negative axial direction. The increased mass flow spillage of Case 1, and its effect on drag, was not seen with Case2 because as discussed in Subsection 3.3, only Case1 extended the MGD interaction
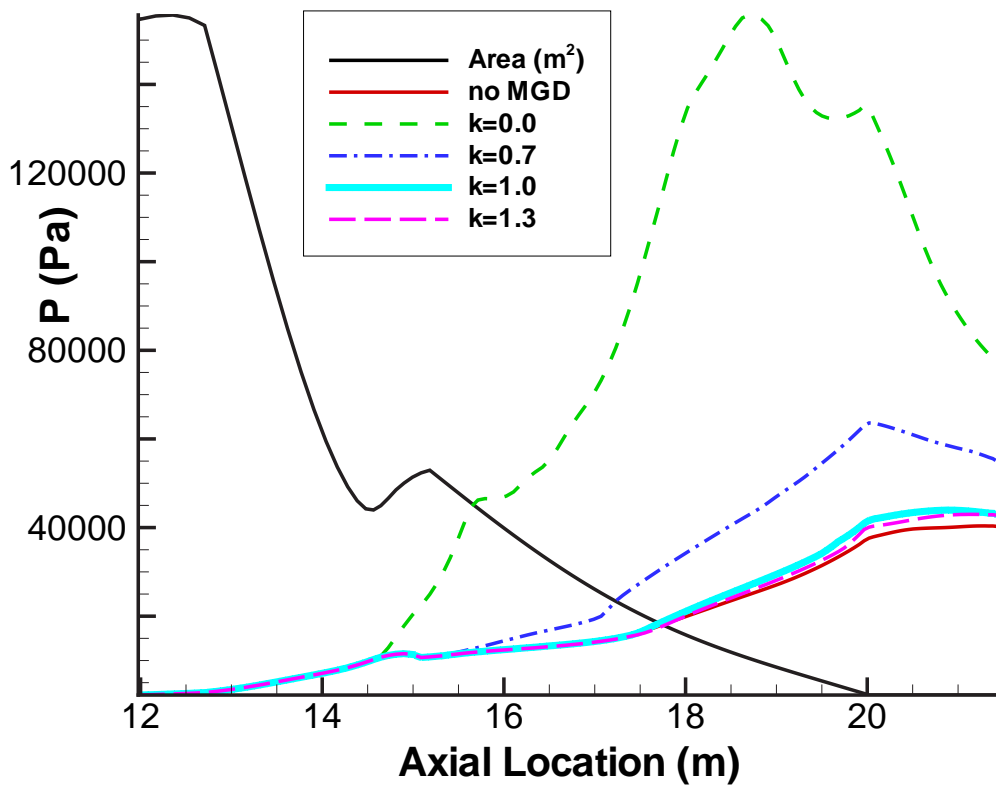
Figure 3.16:   Mean Inlet Pressure for Case 2 with Varying k and $Q = 5$

region upstream of the cowl lip plane. Regarding $\dot{Q}_{ht}$ and the results presented in Fig. 3.18, all cases resulted in heat transfer out of the CV. Just as with Case 1, small decreases were seen with respect to baseline for parameters that resulted in a relatively low level of EM interaction. As seen previously with Case 1, increasing the EM energy interaction always results in increased dissipative losses regardless of whether the device acts as a generator or an accelerator. The trend in heating was the same as for Case 1 in that the greater the departure from $k = 1$, the higher the dissipation and subsequent heating. The peak value was an astounding $465MW$ for the $k = 0, Q = 5$ case.
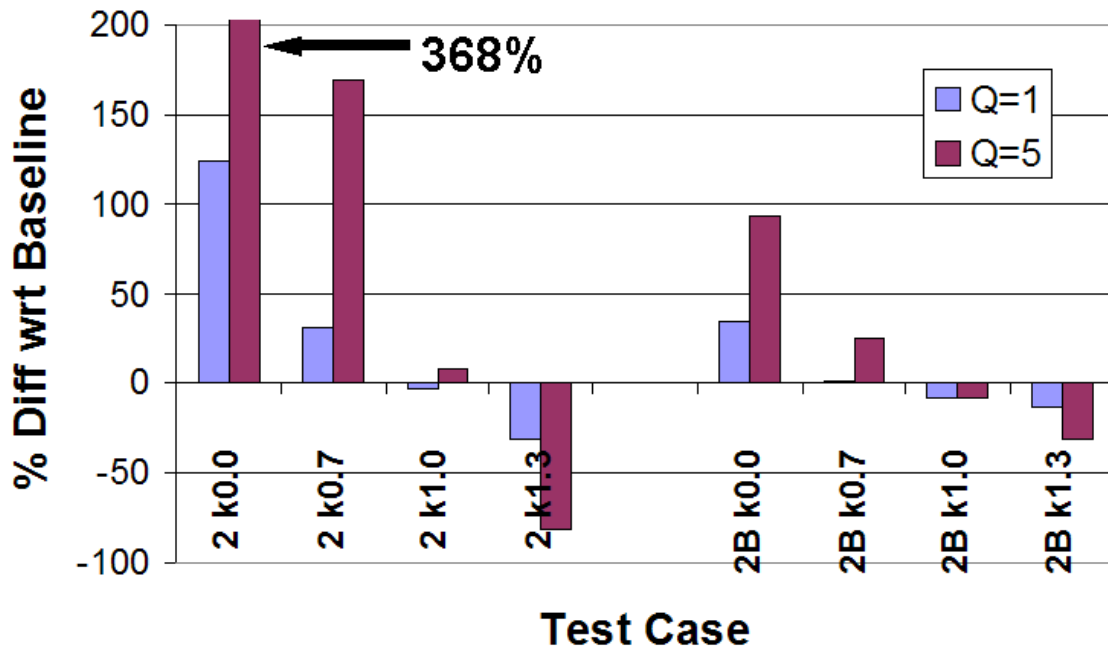
Figure 3.17:   Comparison of Net Inlet Drag for Conductivity Case 2 and 2B

Finally, conductivity and B-field values for this case were comparable to those of Case 1 because the density increased slowly through this portion of the inlet. Values of σ ranged between 0.51 and 0.79 mho/m, and B-fields were on the order of 3.5T for $Q = 1$ and 7.5-9.2T for $Q = 5$. The $k = 0.7$ cases generated a net 39MW and 151MW of electrical power for Q=1 and 5, respectively as depicted in Fig. 3.19. In addition to the $k = 0.7$ cases, the $k = 1, Q = 5$ case demonstrated a net power
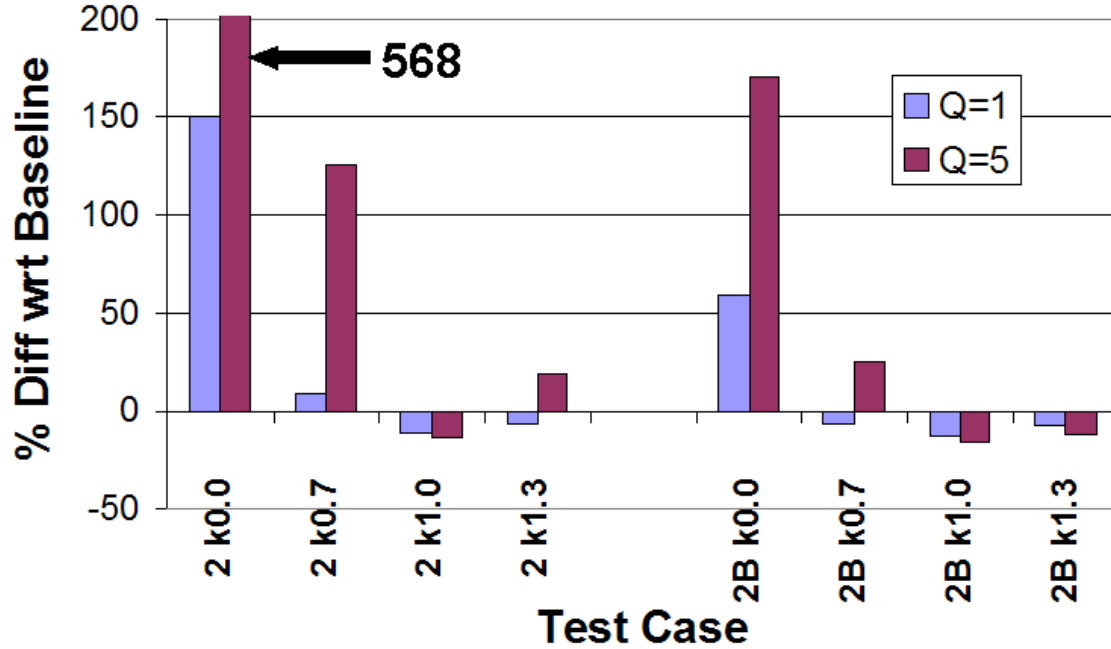
Figure 3.18:   Comparison of Wall Heat Transfer for Conductivity Cases 2 and 2B

generation after ionization of 25MW. These large values of P_{gen} are important as, aside from the ionization power requirements, other electrical power requirements must be met. However, these considerations are beyond the scope of this modelling effort (e.g. electromagnet power supplies and control circuitry). With plasma volume 2.6 times greater than that of Case 1, the required power for ionization was on the order of 4.1–6.3MW for all cases. This was up to approximately 3–4 times the required P_{ion} of Case 1, demonstrating that in light of the axially increasing inlet density, the per unit volume cost of producing the plasma was approximately the same for both Case 1 and 2.

3.7   Results from Conductivity Case 2B

Although not explicitly shown, in reference to Fig. 3.7, one can interpret Case 2B as a combination of the near wall profile of 1B extended axially to the same point as Case 2. Case 2B had a plasma volume of 3.76m^3. Focusing the EM interaction in the near-wall and especially the separated-flow region, resulted in slight increases in the
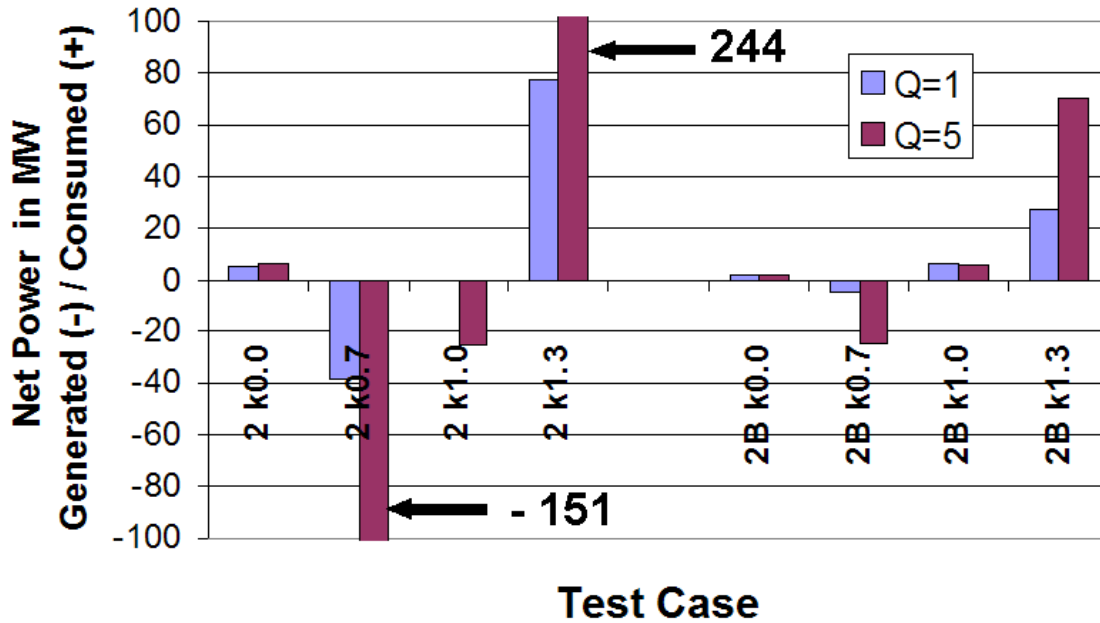
Figure 3.19: Comparison of Net Electric Power Generated/Required for Conductivity Cases 2 and 2B

exit flow pressures and temperatures. Exit Mach numbers decreased by less than 10% with respect to baseline for all but the $k = 0.0, Q = 5$ case which decreased by 20%. Efficiencies relative to the baseline inlet were similar to their Case 1B counterparts as seen in Fig. 3.20. The decreases in efficiency measures were not as great as those for Case 2 because of the smaller, targeted interaction region. Likewise, results from Case 2B did not exhibit the adversely large heat loads and electrical power requirements seen in Case 2.

For example, Table 3.1 compares the $k = 1.3, Q = 5$ accelerator parameters for Cases 2 and 2B. Case 2B had significantly less EM work done, resulting in less heat generation and lower electrical power requirements. Of course, due to the inevitable Joulean dissipation, there was a measurable temperature rise in all instances as also reflected in Table 3.1. Though not shown in Table 3.1, the $k = 0, Q = 5$ parameters had the most negative impact to compression efficiency, with Case 2B being 5.4% less efficient than baseline. Still, this was a marked improvement over the 9.9% lower efficiency for the same parameters applied to Case 2.

(a) Total Pressure Ratio

(b) Dimensionless Entropy Rise

(c) KE Efficiency

(d) Adiabatic Compression Efficiency
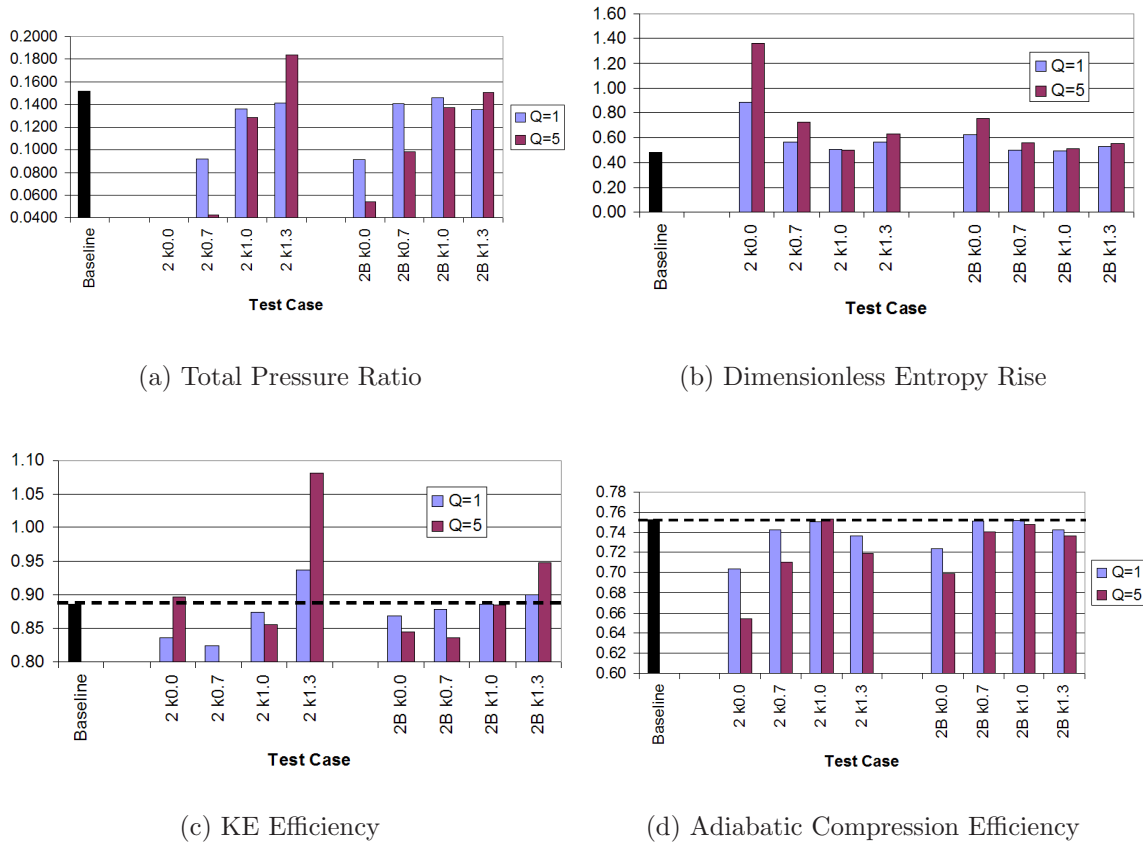
Figure 3.20:   Inlet Efficiency Metrics for Cases 2 and 2B

Table 3.1:   Selected Results for MGD Accelerators, $k = 1.3, Q = 5$

Property	Units	Case 2	Case 2B
p_e	kPa	42.8	41.8
T_e	K	1418	1316
Axial Force	kN	-16.1	-60.1
Wall Heat Transfer, $\dot{Q}_{ht}$	MW	-82.9	-61.4
Net Power	MW	244	70.0
Total Pressure Ratio, π_c	–	0.1838	0.1506
Non-dim Entropy Rise, $\Delta s/C_p$	–	0.6241	0.5522
KE efficiency, η_{KE}	–	1.0805	0.9476
Adiabatic Compression Eff., η_c	–	0.7188	0.7357

The drag results for Case 2B varied widely, but as seen in Fig. 3.17, it was a minimum of 31% less than baseline at $k = 1.3, Q = 5$. A maximum drag value of 94% greater than baseline was obtained for Case 2B when $k = 0.0, Q = 5$. From Fig. 3.18, heat transfer out through the walls was a minimum for $k = 1.0, Q = 5$, with a value of 58MW, 16% less than baseline. Maximum $\dot{Q}_{ht}$ corresponded to the $k = 0, Q = 5$ parameter (as in the other cases), having a specific value of 188MW (177% above baseline). Trends for heating and drag followed the other cases. Conductivity was somewhat higher than in Case 2, ranging between 0.77 and 0.98 mho/m. As with Case 1B, B-fields were on the order of 3T for $Q = 1$ and 6–7.5T for $Q = 5$. Once again, Fig. 3.19 revealed that only the $k = 0.7$ cases demonstrated a net power generation after ionization with Case 2B producing a net of 5MW for $Q = 1$ and 24MW for $Q = 5$. The required power for ionization was on the order of 1.6-1.8MW for all cases. With reference to Fig. 3.20, the MGD accelerators for Cases 2 and 2B showed marginal improvement in flow properties as well as significant drag reduction and increased η_{KE}. However, these cases also required a very large electrical power input. This detrimental factor was reduced to a great extent by localizing the plasma region to the near wall in Case 2B, resulting in an electrical power requirement of 27 and 70MW, for $Q = 1$ and $Q = 5$, respectively.

IV. Application of MGD Energy Bypass to Flowpath

4.1 Introduction

A significant discussion in Chapter I explained the theory behind MGD power generation systems and the energy bypass concept. The reader is referred back to these parts of the document for details. In summary, the MGD energy bypass method is a concept for both producing vehicle electrical power and improving the scramjet's performance. Theoretically, it does this by efficiently removing a portion of the inlet's high stagnation enthalpy, converting it to electrical power, and returning it directly to the expansion system. In this way, the inlet compression is accomplished more efficiently than by the shock train alone. Therefore, the combustor can impart more energy into the flow before running into stagnation temperature limits. This application has been well documented in References [5, 11, 20–22, 26, 34, 40].

The research documented in this chapter tested this application to a level of computational fidelity never before attempted. The next section documents the results for MGD power generation in this engine by first examining the traditional configuration wherein the MGD generator is placed upstream of the combustor. In addition, the concept of combustor-based MGD power generation was explored. This concept, widely pursued in the 1960's in the context of commercial electrical power generation [45], has recently reappeared as a promising concept for scramjet engines as proposed by Macheret, et al [32, 47, 48], among others. The isolator-based generator with the highest electrical power generation was selected for the MGD energy bypass system and several different accelerators were analyzed as described in Section 4.3. Finally, both of these sections are summarized and several conclusions and recommendations specific to this chapter are presented.

4.2 MGD Power Generation

4.2.1 The Conventional Bypass Approach: MGD Power Generation Upstream of the Combustor.   Two approaches were taken to characterize the performance of isolator-based MGD power generation in this engine. The first approach was a

parameter based study similar to that of Chapter III's localized flow control. This approach, which specified the electric field, was done in order to test a wide range of conductivity profiles and load factors (k) at a single interaction parameter ($Q = 1$). The second approach applied higher fidelity to select cases by specifying electrode locations and their electric potential and solving for the resulting electric field and conduction current. In addition to $Q = 1$, the second approach tested the higher magnetic field strengths associated with $Q = 5$. Among other results, it will be shown that electrode placement was critical to successful power generation, and that there was a large difference in performance depending on the load factor, k, and interaction parameter, Q, used.

Numerous runs of the isolator-based MGD generator were performed. Most of these runs specified the electric field. Runs were first delineated by how far the conductivity region extended downstream from the inlet throat as a percentage of the isolator length. Three lengths were tested, 20%, 60% and 100%, as shown in Figures 4.1(a)–(c). As in Chapter III, both a full cross-section profile, referred to here as Case 1E, and a near-wall profile, referred to as Case 2E (e.g. Figure 4.1(d)), were compared. For each conductivity profile, load factors of 0.6, 0.7, and 0.8 were tested. Additional runs were made where the electrode location and electric potential was specified. Since the best results for the specified electric field runs occurred at full isolator length, each electrode run evenly spaced four electrodes along this length as seen in Figure 4.2. Half of the runs placed the electrodes on the +/- Z-faces (referred to as 'K-elec' runs), while the remaining runs placed the electrodes on the +/- Y-faces ('J-elec'). As with the first approach, $k = 0.6$, 0.7, and 0.8 were examined, but this time at both $Q = 1$ and 5. As a final note regarding the problem setup, the baseline inlet without MGD characterized in Subsection 3.1 and used in Chapter III was again used here for determining the performance changes due to the MGD generators. While efficiency metrics are presented in the same manner as in Chapter III, changes in forces and heating are presented as percentage differences with respect to this baseline.

(a) Case 1E-20%

(b) Case 1E-60%

(c) Case 1E-100%

(d) Case 2E-100%
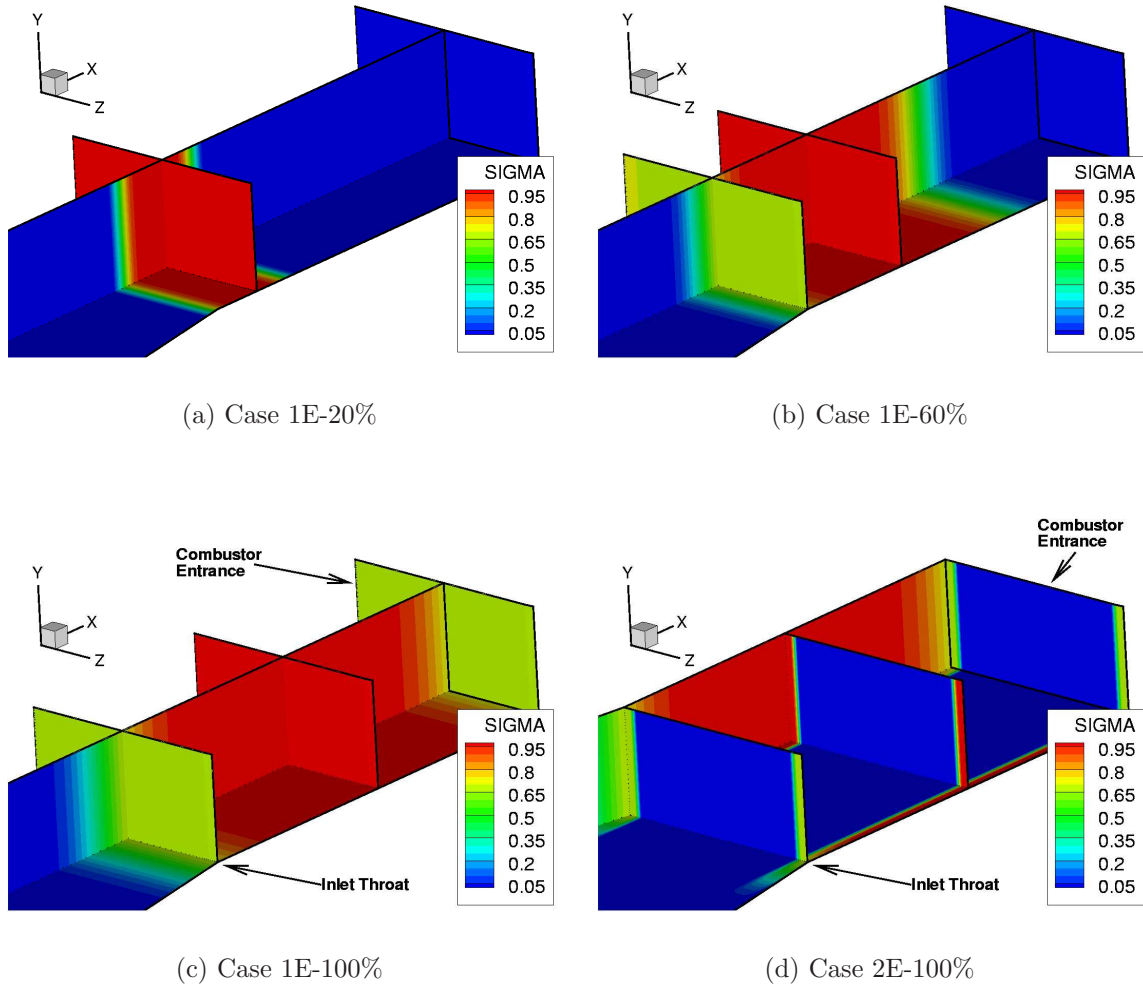
Figure 4.1:   Conductivity Profiles for Isolator-Based Generators with Specified Electric Field

(a) K-elec   (b) J-elec
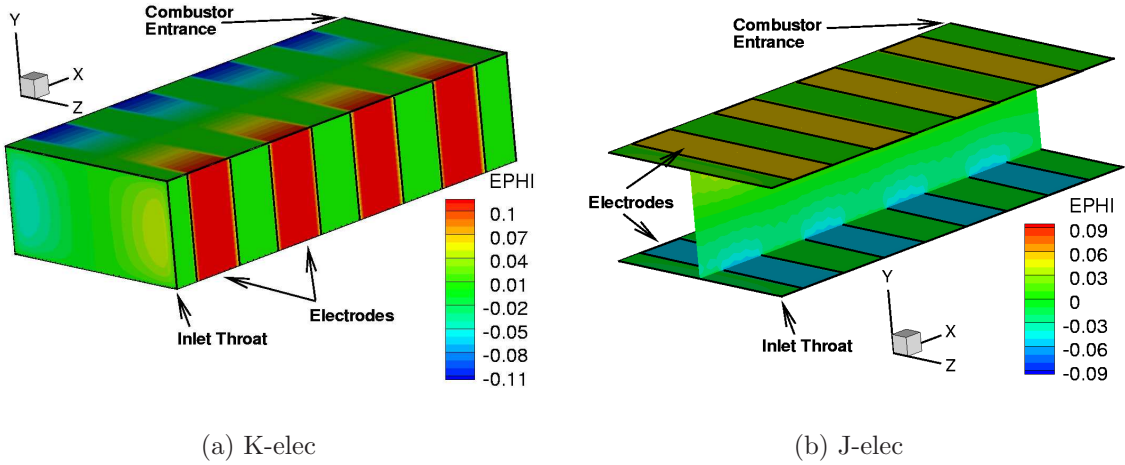
Figure 4.2:   Electrode Configurations for Isolator-Based Generators with Specified Electric Potential

MGD power generation is first and foremost about efficient conversion of flow enthalpy into electrical power. As seen in Figure 4.3, a significant difference was found between methods as well as between individual runs. Beginning with a look at the specified $\vec{E}$-field cases (Case 1E and Case 2E), several expected results were obtained that were in keeping with reduced-order analytical treatments. For example, in an ideal MGD generator, it can be shown that P_{gen} is related to k by Equation 4.1 [45]. Power is then a quadratic function of k with maximum power generation occurring at $k = 0.5$. With respect to a decreasing value of k, all of the results supported this. This included the K-elec cases which experienced a net power consumption; albeit a consumption that decreased as k approached 0.5. The unique circumstances that generated this result will be explained shortly.

$$P_{gen} = \sigma V^2 B^2 k(1 - k) \tag{4.1}$$

Equation 4.1 describes the power generated per unit volume, such that an increase in the plasma volume (e.g. through increasing the axial extent of the generator) made for a substantial increase in power extraction. Comparing Case 1E to 2E further demonstrated that co-locating the bulk of the plasma volume in the center of
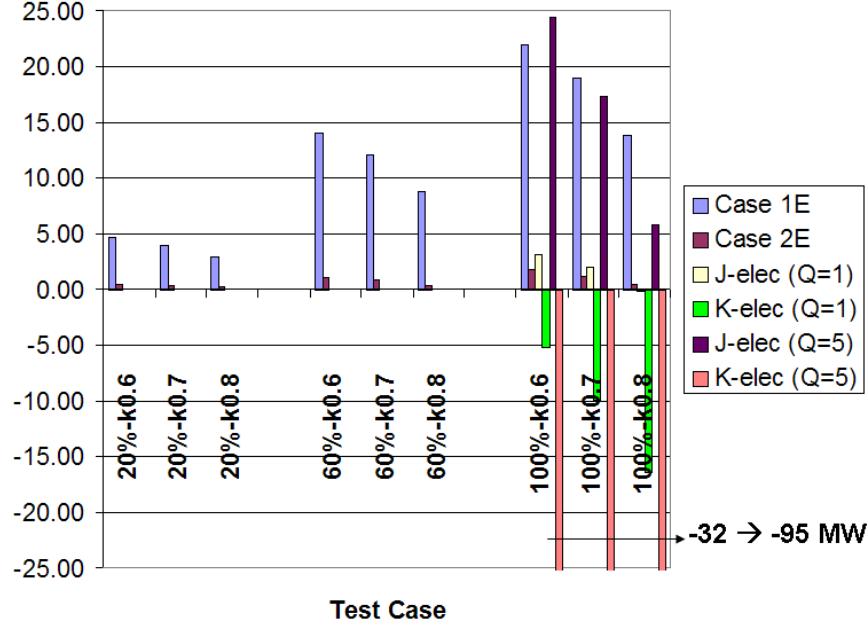
Figure 4.3:   Comparison of Electrical Power Generation/Consumption for Isolator-Based MGD Generators

the channel was a more efficient means of producing power. For example, comparing Cases 2E to 1E where $k = 0.6$, it was seen that, regardless of the axial extent of the generator, the plasma volume ratio was 20%–23%. However, the ratio of total power produced was only 9.5%. Referring again to Equation 4.1, it was clear that the dependence of P_{gen} on V^2 meant that localizing the plasma to the near wall region (where V was relatively small) was relatively inefficient. This result also makes sense from the perspective that the useful work portion of the EM interaction is given by $\vec{V} \cdot (\vec{j} \times \vec{B})$. Therefore, if the plasma volume is limited to the near wall region, where $\vec{V}$ is small in a viscous flow, then relatively little power will be extracted. While current technology is getting close to realizing the centimeter-scale, near wall $\vec{B}$ field strengths of 4.0–4.4T that typified Case 2E, extending these fields across a real scramjet isolator, with distances on the order of a meter, will require a substantial scientific breakthrough. In the end, Case 100%-k0.6 produced the most power but with a required magnetic field strength of 10.5T and conductivity of 0.40mho/m.

4-5

In every respect, the specified $\vec{E}$-field cases behaved as theory would suggest, but at first glance the same could not be said in all regards for the electrode-based cases. As the applied $\vec{B}$-field grew (i.e. Q increasing), the EM-interaction increased roughly as $|\vec{B}|^2$, which was expected. For the J-elec cases, increasing Q from 1 to 5 increased the total P_{gen} by factors from 3–4.5 as k decreased from 0.8 to 0.6. For the K-elec cases, the net power consumption was increased by factors from 7–12 as the nominal load factor decreased from 0.8 to 0.6. As was seen in Figure 4.3 and further quantified here, the net EM-interaction was opposite between the J-elec case which generated electricity and the K-elec case which required additional electricity from an external source. This result was unexpected as only two changes were made between the two configurations. First, the electrodes were placed on different walls and the $\vec{B}$ field was realigned accordingly ($+B_y$ for K-elec and $-B_z$ for J-elec, respectively). Second, a higher electrode potential was used for the K-elec configuration to maintain the same nominal k in spite of the greater distance between the cathode and anode of each electrode pair.

Analysis uncovered the cause for the significantly different performance. For every J-elec run, greater than 50% of the total EM-interaction took the form of work done by Lorentz Forces on the fluid. The opposite was true for all of the K-elec runs, where dissipation accounted for over half of the total interaction. In fact, for the K-elec case of $k = 0.8$ and $Q = 5$, dissipation was 63% of the total interaction, or 1.8 times the corresponding J-elec case. Recall, the EM energy interaction, $\vec{E} \cdot \vec{j}$, consists of the sum of the Joulean dissipation and the rate at which the Lorentz Force does work on the gas as shown again here in Equation 4.2.

$$\vec{E} \cdot \vec{j} = \left|\vec{j}\right|^2 / \sigma + \vec{V} \cdot (\vec{j} \times \vec{B}) \tag{4.2}$$

Furthermore, positive values of $\vec{E} \cdot \vec{j}$, such as occurred with the K-elec configuration mean the external circuit is supplying electricity to the gas, as occurs in an MGD accelerator. However, in an accelerator, the $\vec{V} \cdot (\vec{j} \times \vec{B})$ work term would be positive

with a magnitude that would typically exceed the dissipation. In every K-elec case tested, however, the Lorentz work term was negative. This combination of positive $\vec{E} \cdot \vec{j}$ and negative $\vec{V} \cdot (\vec{j} \times \vec{B})$ is only possible if the applied electric field, $\vec{E}$, is aligned with the induced electric field, $\vec{V} \times \vec{B}$, rather than opposed to it. To verify this was what had occurred, plots of the conduction current, $\vec{j}$, and $\vec{E} \cdot \vec{j}$ were examined for both J-elec and K-elec configurations. Figure 4.4 shows that the K-elec configuration experienced this reversed $\vec{E}$ field condition throughout a significant portion of the plasma volume, but especially near the electrically insulated wall regions between successive electrodes. (Plots for J-elec reflected this condition, also, but to a substantially smaller magnitude and extent than that seen with K-elec.) Due to $\vec{V} \times \vec{B}$, the largest current component acted in the +Z–direction as seen in Figure 4.4(a). Especially strong j_z currents were clearly visible at the electrode-insulator junctions. In light of this, if the configuration was truly acting as an MGD generator, the applied $\vec{E}$ field should have been aligned predominantly in the -Z–direction. Figure 4.4(b), though, reveals large areas where $\vec{E}$ was aligned with $\vec{j}$, confirming that the device was operating as neither a generator nor an accelerator. Rather, external electrical energy was deposited into the gas in a direction that reinforced the -X–directed Lorentz Force and added additional dissipation (i.e. heating).

The obvious issue, then, was determining the mechanism causing substantial portions of the $\vec{E}$ field to reverse from the direction set by the specified electrode potential. A similar effect, but to a lesser degree, was documented by Gaitonde near the MGD generator walls of the AFRL scramjet [11]. The $\vec{E}$ field reversal was attributed to the vanishing induced field that occurred as $\vec{V}$ went to zero at the wall. In order to maintain the overall current direction and continuity, the local $\vec{E}$ field was reversed. It was believed this effect was compounded in the current research for two reasons. First, electric potential differences at the electrode-insulator interface may not have been subjected to the optimum numerical filtering as described in Reference [14]. This numerical instability would account for the large values of current seen at the electrode-insulator interfaces, in turn, leading to increased regions

(a) j$_Z$ Normalized by $V_0 B_0$　　　　(b) $\vec{E} \cdot \vec{j}$ Normalized by $\rho_0 V_0{}^3$
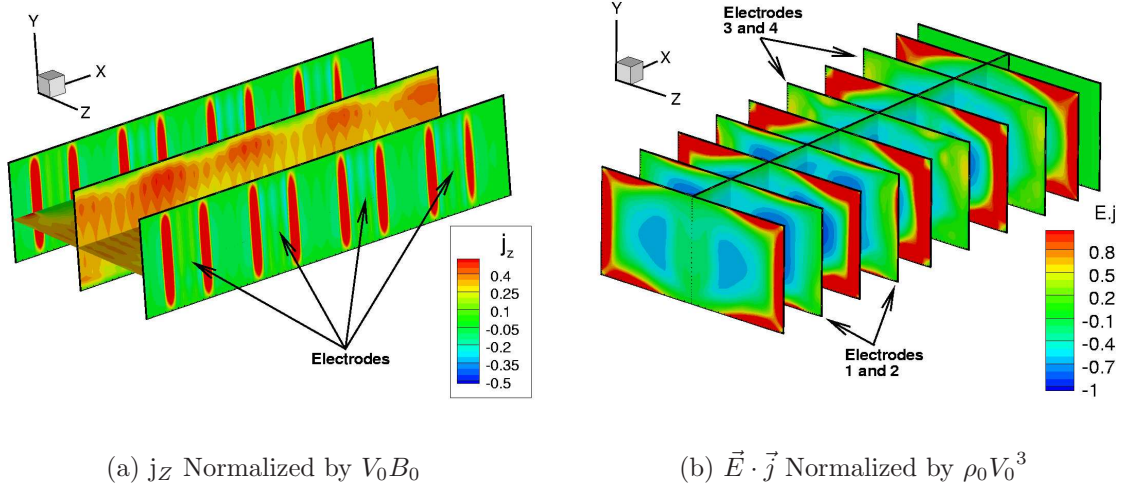
Figure 4.4:　Profiles of Normalized Conduction Current and Net EM Energy Interaction for the K-elec Configuration. ($k = 0.6$(nominal), $Q = 5$)

of reversed $\vec{E}$ fields. Second, the difference between K-elec and J-elec was that they assumed the same mean flow velocity, but because of the larger electrode spacing with K-elec, the applied electrode potential was much greater. This exacerbated the numerical instability along the electrode interface also contributing to the increased areas of $\vec{E}$ field reversal observed. In the end, this effect was obviously not intended and was caused by a numerical issue rather than a fundamental problem with the K-elec configuration. However, it emphasized the inherent difficulty of modelling the EM boundary conditions and highlighted the need to further develop the fidelity of the electrode modelling in the current computational approach.

In spite of this, it was still useful to compare the proper MGD generator performance of the J-elec configuration to that of K-elec. This is because changing flow conditions in a real scramjet will cause significant variations in load factor, leading to difficulties in maintaining proper EM field application. As can be from comparing the net power generation of the J-elec configuration to the consumption of the K-elec configuration (see Figure 4.3), this was exactly the kind of phenomena that made or broke the performance of the realistic MGD generators. The net power consumption with the K-elec cases significantly impacted the flow properties in several

ways as well, due to the large amounts of Joulean dissipation. Figures 4.5(a) and (b) clearly demonstrate this effect on both the decreased Mach number and increased temperature in the isolator with respect to both the baseline case and the J-elec case. The J-elec case did experience additional heating associated with its localized regions of reversed $\vec{E}$ field, but as can be seen, the effect was substantially less. Finally, a look at Figures 4.5(c) and (d) showed that pressure and velocity were also notably impacted. The combined effects of the Joulean dissipation and Lorentz Force (which was significant in the core flow regions of both J-elec and K-elec) acted to drive the mean pressures higher and velocities lower.

Bearing all of this in mind, the performance results came as no surprise. For example, a look at the drag in Figure 4.6(a), showed that all of the $Q = 1$ cases had about 10%–20% more drag than the baseline inlet. However, the $Q = 5$ cases for the J-face electrodes nearly doubled the drag, while the K-face electrodes had closer to 130% of the baseline drag. This last result regarding K-elec was irrespective of the nominal load factor used in determining the electrode potential; being a further manifestation of the mismatched EM field configuration which only contributed increased Lorentz force drag and substantially greater dissipation. This increase in dissipation for the K-elec cases was manifested in heat transfer rates in excess of 130% of baseline for $Q = 5$ as given in Figure 4.6(b). This was more than double that of the J-elec configuration with the same parameters.

Taken together, all of this added drag and heating reduced most of the overall inlet performance measures with respect to the no-MGD baseline. All four of these measures are graphed in Figure 4.7. From this figure, it can be seen that as a stand alone system component the MGD generators reduced the inlet efficiency in every metric with the exception of the kinetic energy efficiency for the K-elec, Q=5 cases. This particular result was spurious and attributable to the inordinate amount of heat put into the isolator that if it were possible to get it back out through an isentropic expansion would result in an increase in kinetic energy. On the positive side, for $Q = 1$ the efficiencies were fairly insensitive to the particular case configuration. From this, it
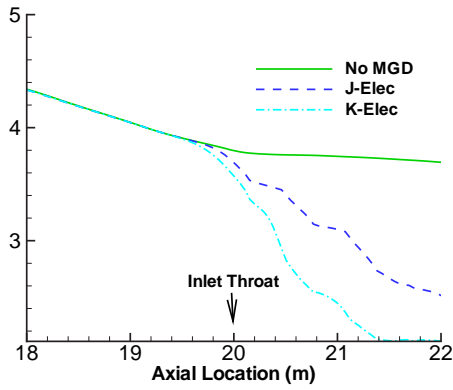
(a) Mach Number
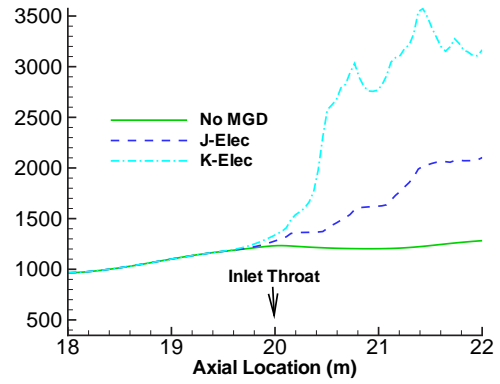
(b) Temperature (K)
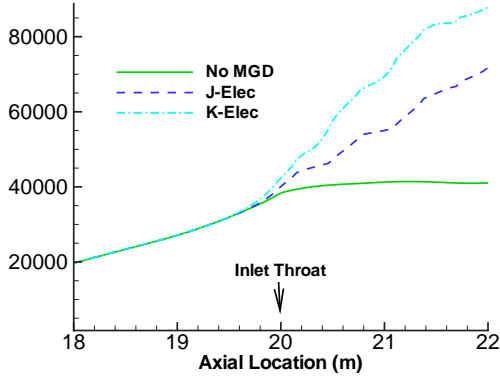
(c) Pressure (Pa)
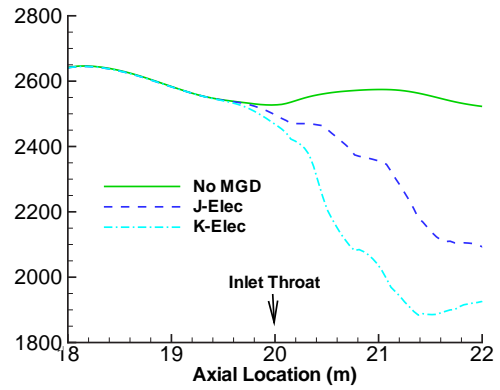
(d) u-Velocity(m/s)

Figure 4.5:   Comparison of Selected Cross-Sectional Averaged Flow Properties for Isolator-Based MGD Power Generation with Specified Electrodes. ($Q = 5$)

(a) Drag
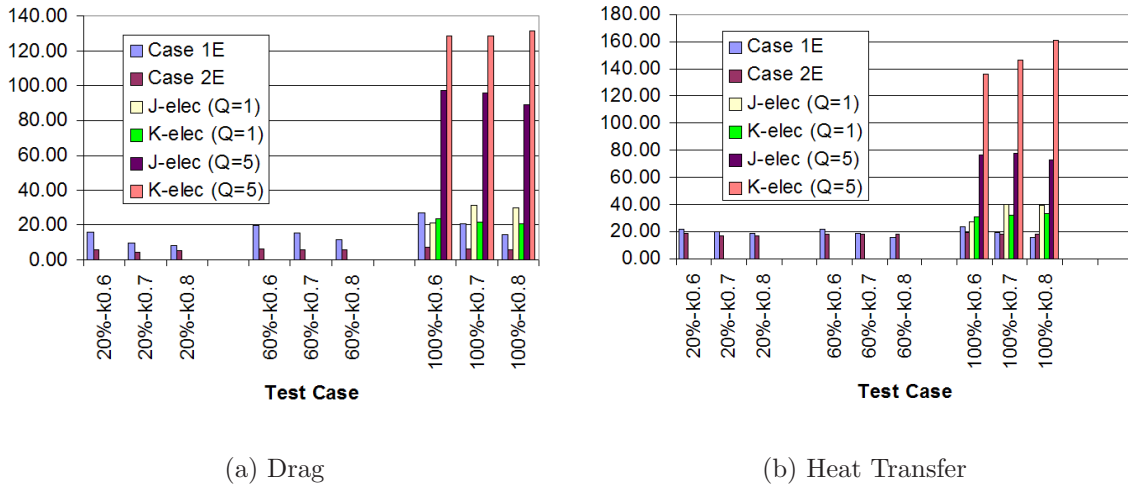
(b) Heat Transfer

Figure 4.6: Increase in Inlet Drag and Heat Transfer Relative to Baseline for Isolator-Based MGD Power Generation

could be concluded that if the primary purpose for MGD power generation is to supply onboard electrical components, smaller generators with lower interaction parameters (i.e. lower system power requirements) should be considered. Moreover, it is more important to focus the interaction region in the core flow, where the useful work was a greater proportion of the overall interaction. However, if the goal is to maximize the work extraction with the goal of bypassing it directly to the expansion system, then the interaction parameter and plasma volume should be maximized. In light of this, it was decided to take the $Q = 5$, J-elec case as the MGD generator portion of the MGD Energy Bypass systems analyzed in Section 4.3. Compared to the same configuration at $Q = 1$, this case produced 7.9 times the electrical power, a result 11% better than the highest generating (but less realistic) specified $\vec{E}$-field models.

(a) π_c

(b) $\Delta s / C_P$

(c) η_{KE}
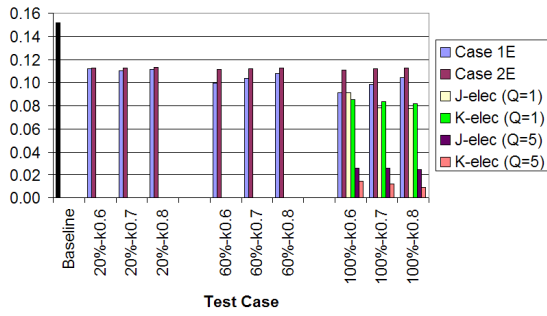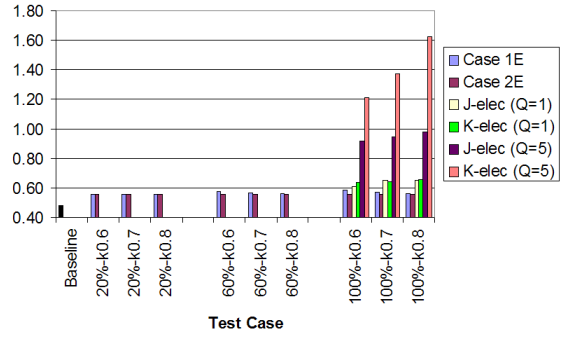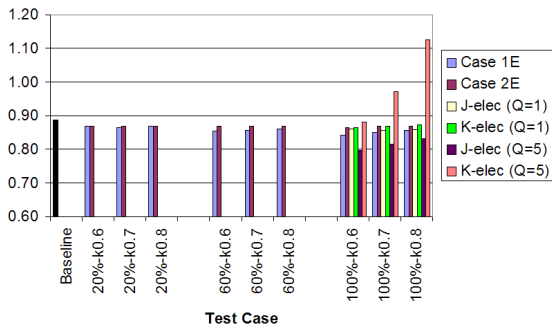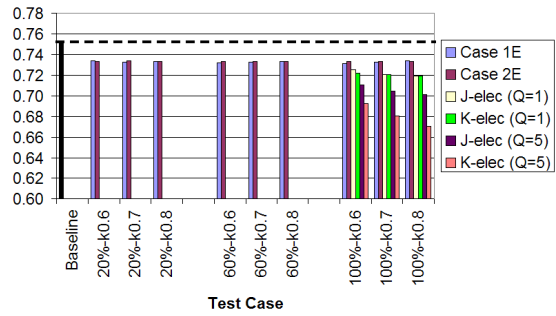
(d) η_C

Figure 4.7: Comparison of Inlet Efficiencies for Isolator-Based MGD Power Generation
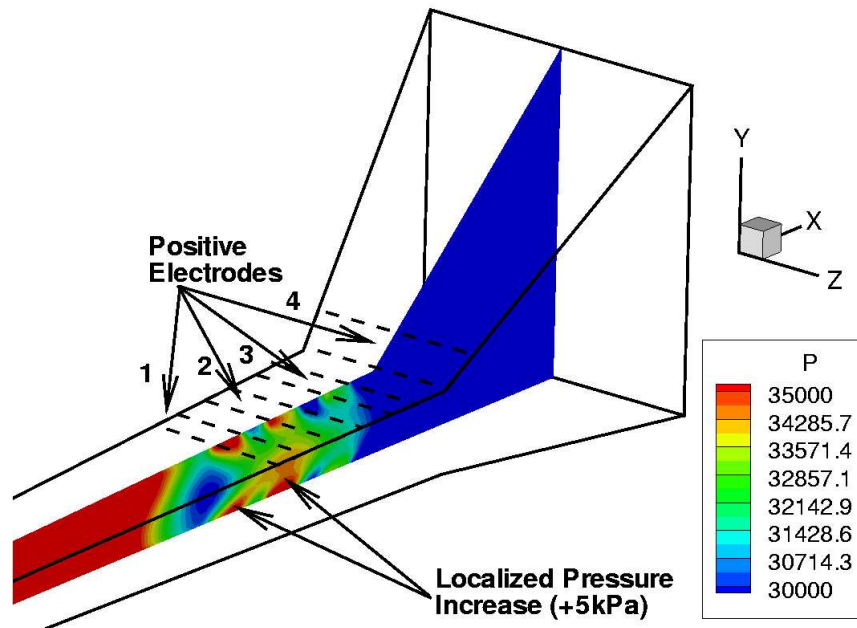
Figure 4.8: Combustor-based MGD Electrode Placement Super-Imposed on Results for Z-Midplane Pressure Contours Using Four Electrode Case (Note: Negative Electrodes Not Shown for Clarity)

4.2.2 Combustor-Based MGD Power Generation. Three configurations were used in order to test the combustor-based alternative to MGD power generation. All three configurations used the higher fidelity approach wherein paired electrodes with specified potential were placed in the aft end of the combustor, and in one case, extending into the beginning of the expansion nozzle. All three configurations used the farthest forward electrode pair (number 1 in Figure 4.8). The configurations were delineated by adding additional electrode pairs such that there was a total of two, three, or four pairs of electrodes, respectively. Because of the issue with $\vec{E}$ field reversal described in the previous section, the electrodes were placed on the +/- Y-faces as seen in Figure 4.8. Every configuration tested assumed $Q = 5$ and a nominal $k = 0.6$ in order to maximize power extraction and provide the same basis for comparison with the isolator-based MGD generators. Each electrode case was initialized from the same converged solution to the finite rate chemistry combustor and run for an identical computational time. Two additional cases were tested for

comparison purposes. The baseline configuration provided the scramjet performance without any MGD flow control, combining the baseline inlet with the finite rate chemistry combustor. Finally, a case (referred to as Isogen) was run using the isolator-based, J-Elec MGD Generator at $k = 0.6$ and $Q = 5$ and the finite rate chemistry modelled combustor. Its purpose was to provide a basis for determining the relative merit of the combustor-based MGD generators.

As expected, the addition of each electrode pair increasingly impacted the combustor flow field properties as shown by Figures 4.9(a)–(d). Taken as a whole, the figure shows that the localized effects caused by subsequent electrode pairs added to the effects due to upstream electrodes creating a cumulative effect on flow properties. This cumulative effect was not simply additive, however. Without a doubt, the single biggest effect was caused by the first electrode pair (EP1). For example, EP1 decreased the average cross-sectional Mach number by 11% to 2.90, but going from EP1 to EP4 only caused an additional 6.9% decline. This effect was visible in the remaining line plots as well, and the cause was clearly evident in the centerline pressure contours of Figure 4.8. In the forward portion of this figure, a decreasing pressure gradient is seen at the trailing end of the combustion reaction zone. Referring to the baseline case in Figures 4.9(c), it was seen the pressure continued to decrease all the way through the end of the domain. However, the addition of the MGD generator in this location caused localized pressure increases in the vicinity of the electrodes, where the conduction current, and therefore, the Lorentz Force was greatest. In fact, the pressure increases coinciding with EP1 and EP2, began to take on the sharply defined appearance of a small shock wave.

Regarding the performance of the combustor-based generators, electrical power generation, axial force, heat transfer, and total pressure ratio were compared to each other as well as the baseline and isolator-based generator cases. To begin, electrical power generation was examined. It was apparent from the results presented in Figure 4.10 that the combustor-based generation was superior in this regard. Foremost, the plasma volume in the 2-Elec case was 56% greater than for the isolator-based

4-14
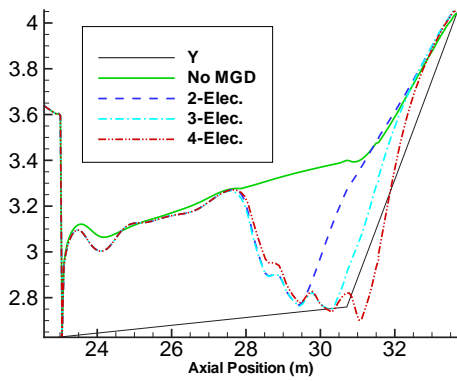
(a) Mach Number
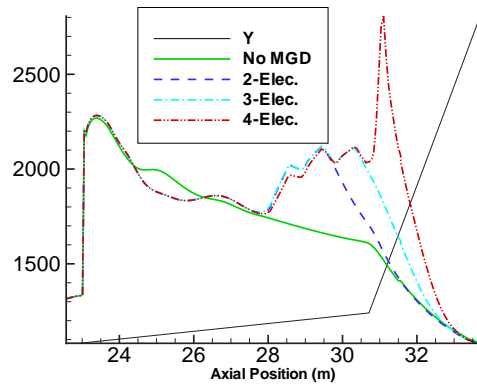
(b) Temperature (K)
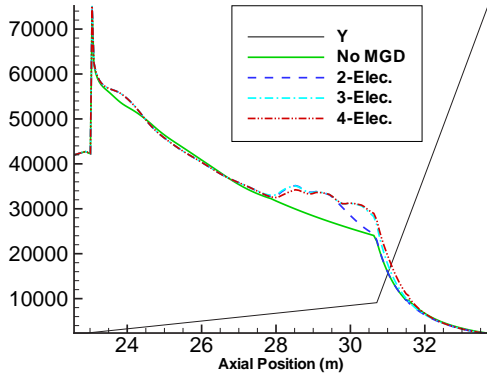
(c) Pressure (Pa)
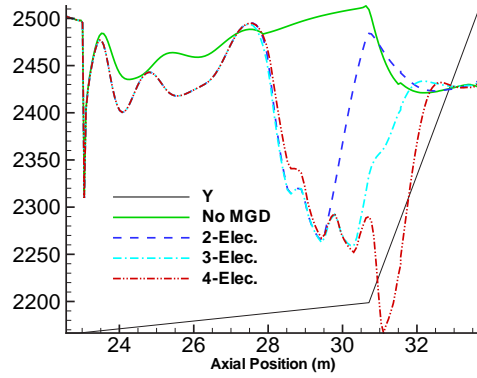
(d) u-Velocity(m/s)

Figure 4.9: Comparison of Selected Cross-Sectional Averaged Flow Properties for Combustor-Based MGD Power Generation with Specified Electrodes. ($Q = 5$)
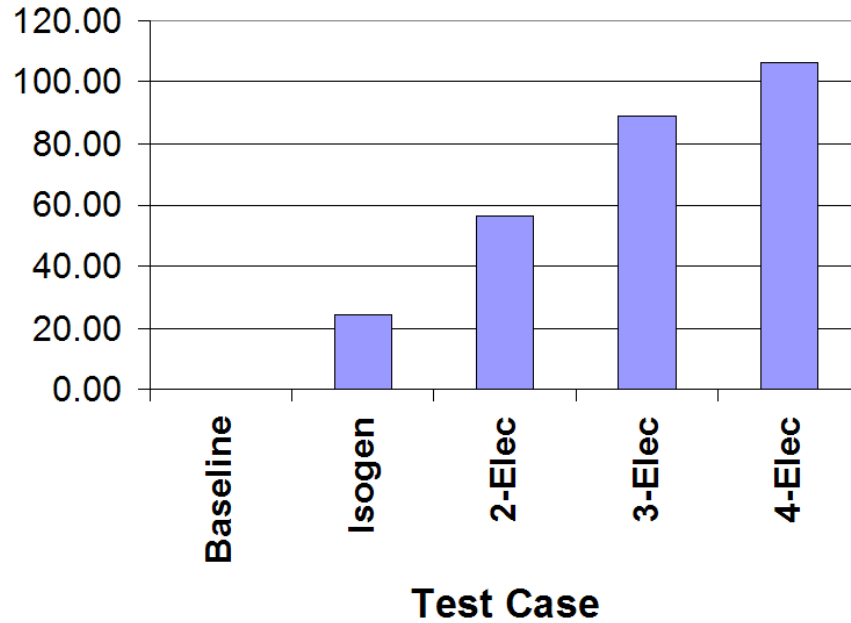
Figure 4.10:   Net Electrical Power Production (in MW) for Combustor-Based MGD Generators

generator, and similarly the 4-Elec case had 3.7 times the isolator-based volume. However, considering the power generation per unit volume, it was seen that the combustor-based cases had values of 12, 10, and 9 MW/m^3 while the isolator-based case only achieved 8 MW/m^3. This was attributable to the lower density in the aft end of the combustor which decreased the ionization cost. For example, the required ionization power density for Elec2 was 578kW/m^3, while for the isolator generator case, it was 991kW/m^3.

Axial force results slightly favored the combustion-based generators as well although the presence of any MGD generator resulted in a total drag increase. Figure 4.11(a) shows that the total axial force (inlet plus combustor and expansion surface) on the baseline engine resulted in an overall drag of 63.7kN. The reasons for this poor performance was that neither the combustor nor expansion surface geometries approached their predicted results. However, it was still useful to use this result to evaluate the MGD system impacts. In this regard, it was seen that the net effect of the isolator-based generator was an overall drag increase of 33% to 84.6kN. The aft

generators performed marginally better in this regard with total drag ranging from 80.0kN – 80.8kN. Heat transfer, however, favored the isolator-based generator, with the exception of the 2-Elec case. As seen in Figure 4.11(b), the heat transfer for both of these cases was 44% above the baseline combustor value. However, in the case of the isolator-based generator this was an added heat load above that already incurred in the isolator. As expected, the remaining combustor-based cases increased their heat transfer into the gas as the number of elctrodes and the volume of the interaction region increased. Finally, a look at total pressure ratio again favored the combustor-based generators. It should be noted, that the ratio for the overall engine was taken as the product of the inlet and combustor ratios. Figure 4.11(c) showed that the overall efficiency with respect to this metric was low for all cases, with a value of 1.3% for the isolator-based generator and 1.8% for both the baseline and combustor-based generator engines. In light of this, the combustor-based generators were felt to be slightly more efficient.
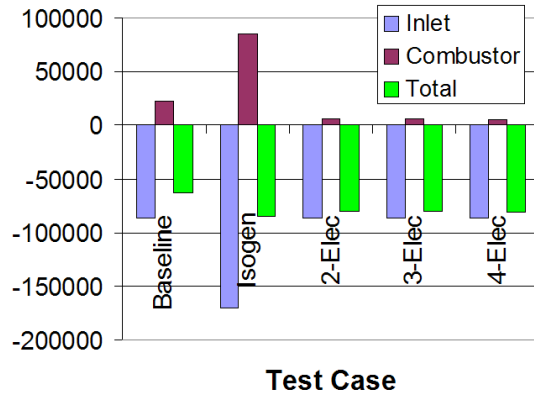
(a) Axial Force (N)
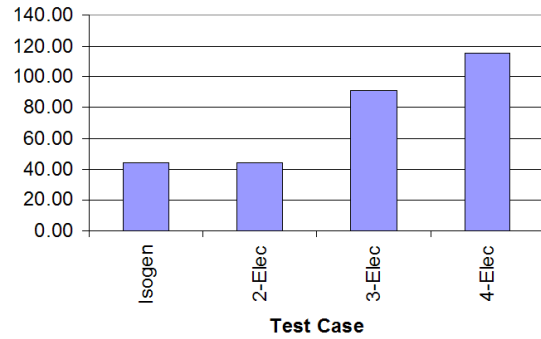
(b) Heat Transfer Relative to Baseline Case
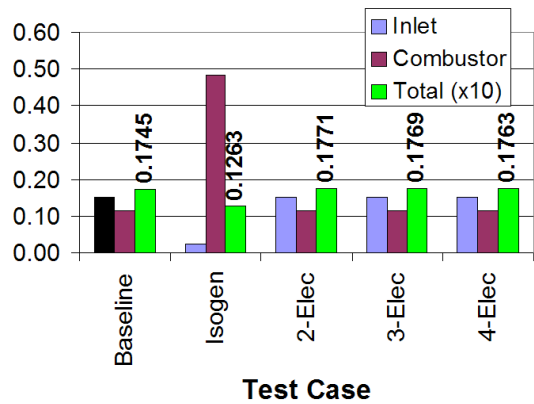
(c) Total Pressure Ratio

Figure 4.11: Comparison of Component and Total Axial Force, Control Volume Heat Transfer, and Total Pressure Ratio for Combustor-Based MGD Power Generation Using Specified Electrodes. ($Q = 5$)

4.3 MGD Flow Acceleration and Energy Bypass

Numerous cases were run with nominal load factors, k, greater than one in an attempt to characterize the effectiveness of MGD acceleration in the aft end of the combustor and obtain a self-powered MGD bypass system. In addition, for every load factor tested interaction parameters, Q, of 1 and 5 were also tested to examine the impact of increasing the $\vec{B}$ field. The specified electrode method was used for all cases using the same configuration as the two and four electrode pair cases from the combustor-based generation runs (refer to geometry in Figure 4.8).

Although all of the cases used a specified electrode potential based on $k > 1$ and a mean value of the local velocity, it was found that values of $k = 1.1$ and $k = 1.3$ actually acted in a generator fashion. Referring back to the discussion of Subsection 4.2.1, what happened in these cases was that the specified potential produced an E-field that, in large areas of the interaction region, had a smaller magnitude than $\vec{V} \times \vec{B}$. In other words, the Lorentz force was acting in the -X direction and net work was being extracted from the flow, consistent with an MGD generator. Of all the cases tested, only those with $k = 2.0$ established a strong enough electric field to cause a net Lorentz force in the +X direction and deposit positive work into the flow. Because of this, only these latter cases were subjected to the complete performance analysis presented here.

Even more so than with the combustor-based MGD generators, it was helpful to look at how the accelerators affected the flow properties. In fact, as seen in the temperature profiles of Figure 4.12(a), the primary effect of all the MGD accelerators was made clearly evident. In all instances, the accelerators increased the static temperature in the interaction region as would be expected. Even at $Q = 1$, the effect was significant with the peak temperature change relative to baseline being 120K and 250K for the 2-Elec and 4-Elec cases, respectively. However, at $Q = 5$ the heating was extreme with peak differences of 800K and 1370K respectively. This last result was 50% greater than the same effect produced by the upstream generator and 65%

greater than the temperature rise due to the fuel injection shock. From this, it was concluded that a significant portion of the energy put back into the flow was in the form of random thermal energy. To verify this, calculations were made to determine the breakdown of the total interaction between Joulean dissipation and useful work. Where typical combustor-based generator results showed useful work extraction made up 67%–75% of the total interaction, accelerators only achieved about 50%–55%, or about half of the entire input was dissipated as heat. Because the electric field is acting to produce a net current flow opposite that induced by the plasma motion, significantly larger overall energy inputs are need to induce a significant useful work contribution. As was seen here, as the energy input increased to accomplish this, the thermal heating likewise increased in greater proportion. This was obviously not a tenable solution, as temperature limits in a real engine would have been easily exceeded well before significant acceleration would be achieved. In fact, examination of the average velocity components (as shown in Figure 4.12(b)) aptly demonstrated this effect. Even with the large interaction of the 4-Elec, $Q = 5$ case the maximum acceleration only achieved a Δu of 85m/s. When accompanied by the heating, the net effect was a decrease in the Mach number entering the expansion nozzle as seen in Figure 4.12(c). For $Q = 5$, this decrease amounted to approximately 0.3.

From the flow field results for the MGD accelerators, it was expected that the performance of the overall MGD bypass configurations tested would be less than what would be needed to account for the increased drag due to the upstream power generation. In fact, the control volume analysis clearly demonstrated that for the configurations tested, none of the bypass systems could achieve an overall engine thrust. Bearing in mind that even the baseline engine suffered a net drag penalty due to the less than optimal combustor and expansion system geometry, it was more useful to once again look at the total axial force relative to the baseline case. As can be seen in Figure 4.13(a), all of the MGD bypass engines demonstrated approximately 33% more net drag than the baseline engine. In effect, the significant drag penalty induced by the MGD generator was not recovered by reinserting electrical energy
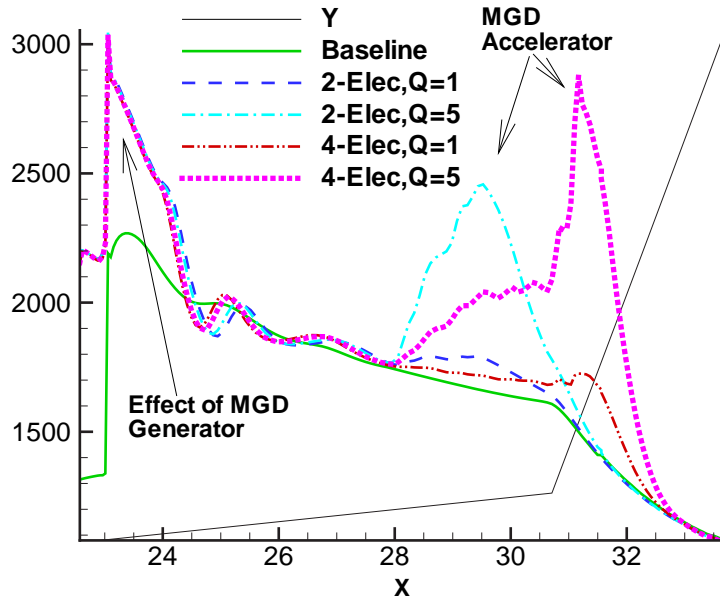
(a) Temperature (K)
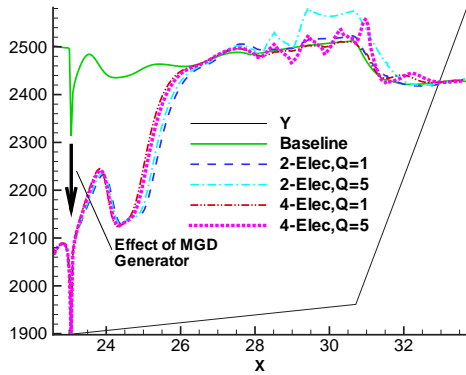
(b) u-Velocity (m/s)
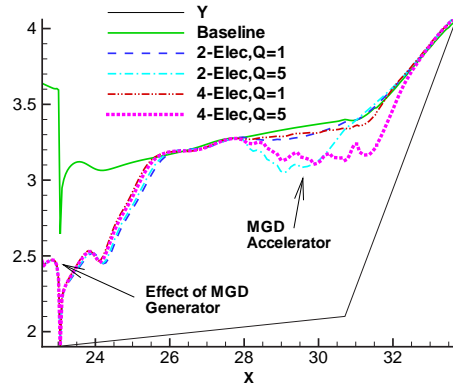
(c) Mach Number

Figure 4.12:   Comparison of Selected Cross-Sectional Averaged Flow Properties for $k = 2.0$ MGD Acceleration with Specified Electrodes.

into the flow. To make matters worse, because the MGD accelerators performed so inefficiently with respect to producing useful work, substantially more energy had to be put into the flow than had been taken out of the generator to produce the results seen. From Figure 4.13(b), it was seen that none of the MGD bypass systems as a whole had a net margin of positive electrical power production. Even the relatively minor interactions from the $Q = 1$ accelerators produced system-level power deficits of 8MW–10MW, which were insignificant compared to the 150MW-class deficits of the $Q = 5$ systems.

In light of these results, it was easy to conclude that for the configurations tested, MGD acceleration was ineffective for improving the performance of this scramjet. Furthermore, when taken as an overall system, the energy bypass concept was unable under any circumstance to be self-powered. While these conclusions must be kept in the context of the segmented Faraday electrodes tested, it is felt that the physics of MGD flow acceleration will in most configurations result in a disproportionate amount of electrical energy being required to produce useful flow work and acceleration. In addition, this work will always be accompanied by a significantly greater fraction of the total energy input being dissipated as heat as compared to a similarly sized MGD generator. However, it is recommended that any future work in the area of MGD acceleration and energy bypass be directed towards the examination of alternative electrode configurations (e.g. Hall current electrodes or diagonally offset Faraday electrodes).

(a) Axial Force (N)
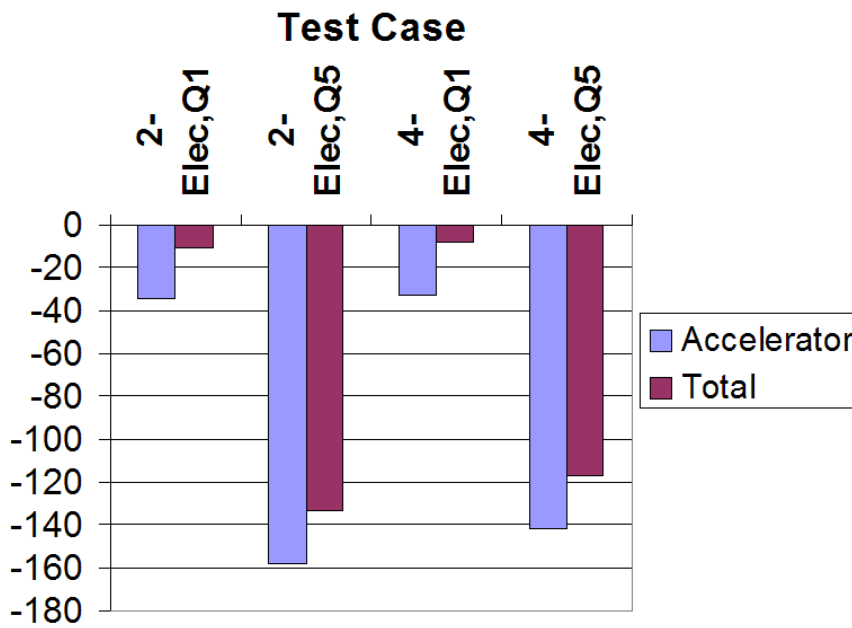
(b) Net Electrical Power in MW (Negative Values Denote Consumption)

Figure 4.13: Comparison of Component and Total Axial Force and Net Electric Power Balance for MGD Energy Bypass Scramjets Using Specified Electrodes.

4.4 Summary of Results, Conclusions and Recommendations Regarding MGD Power Generation and Energy Bypass

Regarding MGD power generation in general, and in particular, generation upstram of the combustor, MW-class electrical power generation was achieved, even for the relatively small interaction parameter of $Q = 1$. However, this positive result came with performance penalties in terms of a drag increase with respect to baseline that varied anywhere from 10% to nearly double the baseline inlet value. This added drag, as well as dissipation induced heating, reduced most of the overall inlet performance measures with respect to the no-MGD baseline. From this, it was concluded that if the primary purpose for MGD power generation is to supply onboard electrical components, smaller generators with lower interaction parameters (i.e. lower system power requirements) should be considered. Moreover, it is more important to focus the interaction region in the core flow, where the useful work was a greater proportion of the overall interaction. However, if the goal is to maximize the work extraction with the goal of bypassing it directly to the expansion system, then the interaction parameter and plasma volume should be maximized. Finally, comparing combustor-based MGD power generation to its isolator-based counterpart revealed that the combustor-based generators performed moderately better, in spite of localized pressure increases in the vicinity of the electrodes which indicated the presence of small shock waves.

During the course of examining the Faraday electrode configurations, it was found that the research code's method of specifying electric potential required making some assumptions regarding the average local flow velocity. The difficulty with this approach is that $\vec{V}$ is never constant and thus there existed electrode configurations with substantial areas of reversed current flow. The net effect was in many configurations MGD generators actually acted as accelerators and vice versa. In light of this fact, it is recommended that future work focus on more accurate methods of modelling the electrode potentials, including consideration of the modelling of the external electric circuit in its entirety.

Finally, with respect to MGD acceleration and specifically the MGD energy bypass concept, it was easy to conclude that for the configurations tested, MGD acceleration was ineffective for improving the performance of this scramjet. Furthermore, when taken as an overall system, the energy bypass concept was unable under any circumstance to be self-powered. Although this research focused on the segmented Faraday electrode configuration, the physics of MGD flow acceleration will in most configurations result in a disproportionate amount of electrical energy being required to produce useful flow work and acceleration. In addition, this work will always be accompanied by a significantly greater fraction of the total energy input being dissipated as heat as compared to a similarly sized MGD generator. However, it is recommended that any future work in the area of MGD acceleration and energy bypass be directed towards the examination of alternative electrode configurations (e.g. Hall current electrodes or diagonally offset Faraday electrodes).

V. Summary, Conclusions, and Recommendations

5.1 Summary

Prior to this work, the analysis of electromagnetic (EM) flow control through the application of magnetogasdynamics (MGD) relied upon simplified analytical treatments and reduced dimensional numerical studies. These key limitations included unrealistic flowpath geometries, calorically perfect gases, and inviscid, 2D flow solvers. As a consequence, not all of the pertinent flow physics were included and thus the conclusions reached were limited in applicability. The effort concluded here contributes directly to the advancement of this research field by removing these limitations, applying the first comprehensive three-dimensional analysis of EM flow control to a flight-sized, scramjet engine.

The starting point for this research was a CFD code developed by the Air Force Research Laboratory (AFRL) to model the full, three-dimensional set of coupled Navier-Stokes and Maxwell's equations [10]. Since the Mach 10 scramjet flow under consideration can be considered a collision-dominated, weakly ionized plasma, the typical MGD assumptions hold. The key assumption in this case was low electrical conductivity and that the magnitude of the applied magnetic field was high. This condition defines the low magnetic Reynold's number regime, which allowed the Lorentz Force and EM interaction to be coupled to the Navier-Stokes' equations as simple source terms. This coupling allows the use of conventional CFD techniques could be employed. For this research, the Roe flux difference splitting scheme with the vanLeer harmonic limiter and central differencing were used for spatial discretization, while an implicit Beam-Warming method was used for temporal discretization. To account for turbulent flow, the widely used $k - \epsilon$ model, modified for use with MGD, was included.

Regarding the CFD modelling of the EM fields, all of the research conducted specified the magnetic flux density, $\vec{B}$, at all points and assumed it was invariant in both time and space. The plasma conductivity, σ, was time invariant as well, with a scalar value whose spatial growth and decay was held constant by a three-

dimensional Gaussian distribution. Two methods of calculating the electric field, $\vec{E}$, were employed. The first approach was the same as for $\vec{B}$, wherein $\vec{E}$ was initialized and then held invariant. This approach was simpler to implement and had a distinct advantage in lower computational expense. However, the solutions obtained demonstrated that it was likely to produce less realistic results. The second approach used a higher fidelity approach, specifying the locations and electric potential for wall-based electrodes. A Poisson solver was used with this approach to enforce current continuity and obtain the $\vec{E}$ field. The advantage of this method was that it created an $\vec{E}$ field that was coupled to the flow, such that as the EM interaction altered the flow, the flow would simultaneously change the $\vec{E}$ field until reaching equilibrium. This results in a more realistic capturing of the flow physics. More importantly, accurately capturing the physics at electrode-insulator boundaries presented problems with some MGD device configurations, as did difficulties in applying optimized numerical filtering.

As a final note, all of the electrode-based models tested used a segmented Faraday configuration where paired electrodes of opposite potential were placed on opposing wall boundaries. Because of this configuration, Hall current effects were not included in this research.

Two significant additions to the existing code were made to support the goals of this research. The first was the creation of a post-CFD analysis tool that allowed for a dimensional analysis of the EM impacts to the system and its performance. Key to this addition was the inclusion of an electron beam model and routines to perform cross-sectional and cell-based averages of flow and EM properties. These results were then cast into a form suitable for taking a control volume approach that was used to determine overall performance values, e.g. forces, heat transfer, and total pressure ratios.

The second major addition was the development and verification of a finite rate thermochemistry model. The primary purpose for undertaking this portion of the research effort was because stable, efficient combustion has traditionally been

one of the greatest challenges to achieving scramjet propulsion. A portion of this research broke new ground in demonstrating the first coupling of a finite rate chemistry and MGD solver for scramjet applications. In addition, the coupling algorithm was purposefully generalized such that it could be used or turned off as needed, allowing computational expense to be balanced against a particular application's requirements. The successful implementation of this computational tool, overcame two significant shortfalls in the AFRL research code: (1) the major assumption the gas was non-reactive air, and (2) chemical combustion could only be represented by a simple volumetric heating rate source term in the energy equation.

Culminating the research effort, a detailed computational analysis of this engine in the context of both localized MGD flow control applications and the MGD energy bypass system were explored. Regarding local EM flow control, this research explored the possibility of mitigating a region of separated flow within the internal inlet and increasing the average pressure entering the combustor. Two MGD concepts were considered to address this issue: increasing pressure in the cowl shoulder region to better match that of the reflected shock, or increasing flow momentum in the boundary layer to overcome the adverse pressure gradient. A parametric study tested these concepts by varying the spatial distribution of the plasma region, the load factor, k, and the interaction parameter, Q. In summary, localized MGD flow control was marginally successful in raising the average pressure entering the combustor, and even more successful at reducing overall inlet drag.

The system-level MGD research was tested to a level of computational fidelity never before attempted. Three distinct applications were investigated: (1) stand-alone MGD power generation performed upstream of the combustor, (2) stand-alone combustor-based MGD power generation, and (3) a full MGD energy bypass system. Regarding MGD power generation in general, and in particular, generation upstream of the combustor, MW-class electrical power generation was achieved, even for the relatively small interaction parameter of $Q = 1$. However, this positive result came with performance penalties in terms of a drag increase with respect to baseline that

varied anywhere from 10% to nearly double the baseline inlet value. This added drag, as well as dissipation induced heating, reduced most of the overall inlet performance measures with respect to the no-MGD baseline. Comparing combustor-based MGD power generation to its isolator-based counterpart revealed that the combustor-based generators performed moderately better, in spite of localized pressure increases in the vicinity of the electrodes which indicated the presence of small shock waves.

With respect to MGD acceleration and specifically the MGD energy bypass concept, none of the configurations tested improved the performance of this scramjet with respect to net axial force. Rather, as compared to the baseline engine all of the bypass engines experienced a net drag increase of approximately 33%. Furthermore, none of the bypass engines could be considered self-powered. In every case, the power produced by the most powerful generator tested was insufficient to both ionize the flow and supply the power required by the MGD accelerators. While these conclusions must be kept in the context of the segmented Faraday electrodes tested, it is felt that the physics of MGD flow acceleration will in most configurations result in a disproportionate amount of electrical energy being consumed to produce useful flow work and acceleration. In addition, the flow work will always be accompanied by a significantly greater fraction of the total energy input being dissipated as heat as compared to a similarly sized MGD generator.

5.2   Conclusions

Based upon this research effort, the following conclusions were reached:

1. *The loosely coupled approach to incorporate finite rate chemistry was very successful with respect to modelling supersonic combustion flow problems and is recommended over the existing polynomial gamma and heat source term approaches for these problems.* With regard to the actual scramjet modelling done, the inclusion of combustion chemistry resulted in the most accurate representation of a real engine.

2. *As a consequence, this successful addition to the AFRL computational electromagnetics code provides the only open-source model of fuel injection, mixing and combustion for MGD flow control applications.*

3. *The placement of the EM interaction region, and in particular the electrodes, is critical to successful exploitation of this technology.* The extent of the flow-EM interaction is only fully realized when the inherent complexity of the 3D, viscous flow physics is taken into account. 1D or 2D, inviscid solutions by themselves are inadequate for accurately capturing the impacts to performance in the scramjet engine. As an example, placement of the EM-interaction region near the wall was the most important factor in determining the wall heat transfer, and targeting the conductivity to this region was a relatively efficient method of limiting drag increases.

4. *MGD electrical power generation for the purpose of powering the vehicle's on-board electrical systems, to include the ionization source and any electromagnet requirements, is certainly feasible with a flight-sized engine.* This assumes of course that the weight and complexity of the magnet and associated ionization and control system does not prove prohibitive. For many of the MGD generator cases, MW-class electrical power generation was achieved, verifying the results of previous research. However, tying back to the previous conclusion, electrode placement was critical to successful power generation and there was a large difference in performance depending on the k and Q used.

5. *The use of an MGD accelerator to locally increase flow momentum was an effective approach to improve flow into the isolator of this scramjet model.* Although it only slightly increased the flow pressure going into the isolator, MGD acceleration, particularly for Case 2B, was able to efficiently reduce the net inlet drag. It did this while minimizing the increase in heat transfer and decrease in overall efficiency measures. This was due primarily to increasing the flow momentum as it passed through the sidewall expansion into the inlet throat.

6. *Combustor-based MGD power generation was superior to the inlet-based approach with respect to power density and overall engine efficiency.* For electrical power generation, then, an approach similar to that of ground-based, combustion-fired MGD generators should be pursued.

7. *For the electrode configurations tested, MGD acceleration was ineffective for improving the performance of this scramjet. Furthermore, when taken as an overall system, the energy bypass concept was unable under any circumstance to be self-powered.* MGD acceleration was shown to be ineffective in improving overall performance, with all of the bypass engines having approximately 33% more drag than baseline and none of them achieving a self-powered state. In light of this, it is difficult to conceive of a viable MGD energy bypass system.

5.3 Recommendations for Future Research

1. Future work in the area of MGD acceleration and energy bypass should be directed towards *the examination of alternative electrode configurations* (e.g. Hall current electrodes or diagonally offset Faraday electrodes).

2. In this regard, *a more detailed method of modelling the electrode potential should be undertaken that better accounts for the electrode-insulator boundary condition.* This is necessary to eliminate detrimental effects such as near wall reversal of the $\vec{E}$ field that was seen with some electrode configurations.

3. In conjunction with the two prior recommendations, *the optimum distance off the wall to target the electron beam ionization should be investigated further.*

4. Finally, *long term research in this area should include modelling of the external electric circuit to understand the dynamic response of these flow control systems.* This modelling should include, as a minimum, a detailed analysis of the ionization and magnetic field generator power requirements as well as the load presented by the vehicle's overall electrical system.

Bibliography

1. *Stopping Powers for Electrons and Positrons*. Technical report, International Commission on Radiation Units and Measurements, 1984.

2. Bityurin, V.A., A.N. Bocharov, and J.T. Lineberry. "Results of Experiments on MHD Hypersonic Flow Control". *35th AIAA Plasmadynamics and Lasers Conference*, 1–15. AIAA, 2004.

3. Brichkin, D.I., A.L. Kuranov, and E.G. Sheikin. "The Potentialities of MHD Control for Improving Scramjet Performance". 1–11. AIAA 1999-4969.

4. Bruno, C. and P.A. Czysz. *An Electro-Magneti-Chemical Hypersonic Propulsion System*. Technical report, AIAA, 1998.

5. Burakhanov, B.M., A.P. Likhachev, S.A. Medin, V.A. Novikov, V.I. Okunev, V.Y. Rickman, and V.A. Zeigarnik. "Advancement of Scramjet Magnetohydrodynamic Concept". *Journal of Propulsion and Power*, 17(6):1247–1252, 2001.

6. Cockrell, C.E.J., W.C. Engelund, R.D. Bittner, T.N. Jentink, A.D. Dilley, and A. Frendi. "Integrated Aeropropulsive Computational Fluid Dynamics Methodology for the Hyper-X Flight Experiment". *Journal of Spacecraft and Rockets*, 38(6):836–843, 2001.

7. D'Ambrosio, D. and D. Giordano. "Electromagnetic Fluid Dynamics for Aerospace Applications. Part I: Classification and Critical Review of Physical Models". *35th AIAA Plasmadynamics and Lasers Conference*, 1–14. AIAA, 2004.

8. Dornheim, M.A. "A Breath of Fast Air". www.aviationnow.com, 2004.

9. Evans, J.S. and Jr. Schexnayder, C.J. "Influence of Chemical Kinetics and Unmixedness on Burning in Supersonic Hydrogen Flames". *AIAA Journal*, 18(2):188–193, 1980.

10. Gaitonde, D.V. "Development of a Solver for 3-D Non-Ideal Magnetogasdynamics". *30th AIAA Plasmadynamics and Lasers Conference*, 1–15. AIAA, 1999.

11. Gaitonde, D.V. "Three-Dimensional Flow-Through Scramjet Simulation with MGD Energy Bypass". *41st AIAA Aerospace Sciences Meeting and Exhibit*, 1–19. AIAA, 2003.

12. Gaitonde, D.V. and J. Poggie. "Simulation of Magnetogasdynamic Flow Control Techniques". AIAA, 2000.

13. Gaitonde, D.V. and J. Poggie. "An Implicit Technique for 3-D Turbulent MGD with the Generalized Ohm's Law". *32nd AIAA Plasmadynamics and Lasers Conference*, 1–17. AIAA, 2001.

14. Gaitonde, D.V. and J. Poggie. "Elements of a Numerical Procedure for 3-D MGD Flow Control Analysis". *40th AIAA Aerospace Sciences Meeting and Exhibit*, 1–17. AIAA, 2002.

15. Heiser, W.H. and D.T. Pratt. *Hypersonic Airbreathing Propulsion*. AIAA Education Series. AIAA, 1994.

16. Holland, S.D. "A Computational and Experimental Investigation of a Three-Dimensional Hypersonic Scramjet Inlet Flow Field", 1991.

17. Holland, S.D. and J.N. Perkins. "Contraction Ratio Effects in a Generic Three-Dimensional Sidewall Compression Scramjet Inlet: A Computational and Experimental Investigation". *AIAA 22nd Fluid Dynamics, Plasma Dynamics, and Lasers Conference*, 1–18. AIAA, 1991.

18. Hughes, W.F. and F.J. Young. *The Electromagnetodynamics of Fluids*.

19. Kuranov, A.L., V.V. Kuchinsky, and E.G. Sheikin. "Scramjet with MHD Control under "AJAX" Concept. Requirements for MHD Systems." *32nd AIAA Plasmadynamics and Lasers Conference*, 1–11. AIAA, 2001.

20. Kuranov, A.L. and E.G. Sheikin. "MHD Control on Hypersonic Aircraft under "AJAX" Concept. Possibilities of MHD Generator". *40th AIAA Aerospace Sciences Meeting and Exhibit*, 1–11. AIAA 2002-0490.

21. Kuranov, A.L. and E.G. Sheikin. "The Potential of MHD Control for Improving Scramjet Performance". *30th AIAA Plasmadynamics and Lasers Conference*, 1–9. AIAA 1999-3535.

22. Kuranov, A.L. and E.G. Sheikin. "Magnetohydrodynamic Control on Hypersonic Aircraft Under "Ajax" Concept". *AIAA Journal of Spacecraft and Rockets*, 40(2):174–182, 2003.

23. Lindsey, M.F., R.J. McMullan, and D.V. Gaitonde. "Development of a Realistic 3-D Scramjet Flowpath for MGD Energy Bypass". AIAA 2005-1178, 2005.

24. Linstrom, P.J. and W.G. Mallard (editors). *NIST Chemistry WebBook, NIST Standard Reference Database Number 69*. National Institute of Standards and Technology, Gaithersburg MD, 20899, 1995.

25. Litchford, R.J., J.W. Cole, V.A. Bityurin, and J.T. Lineberry. *Thermodynamic Cycle Analysis of Magnetohydrodynamic-Bypass Hypersonic Airbreathing Engines*. Technical report, NASA TP-2000-210387, 2000.

26. Litchford, R.J., J.W. Cole, and J.T. Lineberry. "Thermodynamic Cycle Analysis of Magnetohydrodynamic-Bypass Hypersonic Airbreathing Engines". *Journal of Propulsion and Power*, 17(2):477–480, 2000.

27. Macheret, S.O., R.B. Miles, and G.L. Nelson. "Feasibility Study of a Hybrid MHD/Radiatively Driven Facility for Hypersonic Ground Testing". AIAA 1997-2429, 1997.

28. Macheret, S.O., M.N. Shneider, and R.B. Miles. "Potential Performance of Supersonic MHD Power Generators". *39th AIAA Aerospace Sciences Meeting and Exhibit*, 1–24. AIAA 2001-0795.

29. Macheret, S.O., M.N. Shneider, and R.B. Miles. "Energy-Efficient Generation of Nonequilibrium Plasmas and Their Applications to Hypersonic MHD Systems". AIAA 2001-2880, 2001.

30. Macheret, S.O., M.N. Shneider, and R.B. Miles. "Magnetohydrodynamic Control of Hypersonic Flows and Scramjet Inlets Using Electron Beam Ionization". *AIAA Journal*, 40(1):74–81, 2002.

31. Macheret, S.O., M.N. Shneider, and R.B. Miles. "Modeling of Air Plasma Generation by Repetitive High-Voltage Nanosecond Pulses". *IEEE Transactions of Plasma Science*, 30(3):1301–1314, 2002.

32. Macheret, S.O., M.N. Shneider, D.M. Van Wie, and R.B. Miles. "MHD Power Generation in Scramjet Engines in Conjunction with Inlet Control". *42nd AIAA Aerospace Sciences Meeting and Exhibit*, 1–24. 2004.

33. McEldowney, B., R. Meyer, N. Chintala, and A.I. V. "Measurements of Electrical Parameters of a Supersonic Non-Equilibrium MGD Channel". *34th AIAA Plasmadynamics and Lasers Conference*, 1–14. AIAA, 2003.

34. Mehta, U.B., D.W. Bogdanoff, and C. Park. *A Perspective on a Combined Magneto-Hydrodynamic-Scramjet Engine*. Technical report, NASA, 2001.

35. Meyer, R., B. McEldowney, N. Chintala, P. Palm, and I.V. Adamovich. "Experimental Studies of Plasma Assisted Ignition and MGD Supersonic Flow Control". *41st AIAA Aerospace Sciences Meeting and Exhibit*. AIAA, 2003.

36. Mitchner, M. and C. Kruger. *Partially Ionized Gases*. John Wiley and Sons, 1973.

37. NASA. "Guinness World Records Recognizes NASA X-43A Speed Record". NASA Dryden News Releases, 2004.

38. NASA. "Faster Than a Speeding Bullet: Guinness Recognizes NASA Scramjet". NASA News Release: 05-156, 2005.

39. Nishihara, M., R. Meyer, M. Cundy, W.R. Lempert, and I.V. Adamovich. "Development and Operation of a Supersonic Nonequilibrium MHD Channel". *35th AIAA Plasmadynamics and Lasers Conference*, 1–19. AIAA, 2004.

40. Park, C., D.W. Bogdanoff, and U.B. Mehta. "Theoretical Performance of Frictionless Magnetohydrodynamic-Bypass Scramjets". *Journal of Propulsion and Power*, 17(3):591–598, 2001.

41. Poggie, J. and D.V. Gaitonde. "Magnetic Control of Hypersonic Blunt Body Flow". *38th AIAA Aerospace Sciences Meeting and Exhibit*, 1–15. AIAA, 2000.

42. Poggie, J. and D.V. Gaitonde. "Computational Studies of Magnetic Control in Hypersonic Flow". *39th AIAA Aerospace Sciences Meeting and Exhibit*, 1–12. AIAA, 2001.

43. Poggie, J. and D.V. Gaitonde. "Magnetic control of flow past a blunt body: Numerical validation and exploration". *Physics of Fluids*, 14(5):1720–1731, 2002.

44. Riggins, D.W. "Analysis of the Magnetohydrodynamic Energy Bypass Engine for High-Speed Airbreathing Propulsion". *AIAA Journal of Propulsion and Power*, 20(5):779–792, 2004.

45. Rosa, R.J. *Magnetohydrodynamic Energy Conversion*. McGraw-Hill, 1968.

46. Sato, H. "The Hall Effect in the Viscous Flow of Ionized Gas between Parallel Plates under Transverse Magnetic Field". *J. Phys. Soc. of Japan*, 16(7):1427–1433, July 1961.

47. Shneider, M.N. and S.O. Macheret. "Modeling of Plasma Virtual Shape Control of Ram/Scramjet Inlet and Isolator". *35th AIAA Plasmadynamics and Lasers Conference*, 1–19. AIAA 2004-2662, 2004.

48. Shneider, M.N. and S.O. Macheret. "Hypersonic Aerodynamic Control and Thrust Vectoring by Nonequilibrium Cold-Air MHD Devices". AIAA 2005-0979, 2005.

49. Sutton, G.W. and A. Sherman. *Engineering Magnetohydrodynamics*. McGraw-Hill, 1965.

50. Turchak, A., A. Kuranov, and A. Korabelnikov. "Hypersonic Technologies of the "AJAX" Concept". AIAA 2002-5184, 2002.

51. White, F.M. *Fluid Mechanics*, chapter 3. McGraw-Hill, 2 edition, 1986.

REPORT DOCUMENTATION PAGE

1. REPORT DATE *(DD–MM–YYYY)*	2. REPORT TYPE	3. DATES COVERED *(From — To)*
10–04–2006	AFOSR Final Report	Jan 2003 — Dec 2005

4. TITLE AND SUBTITLE	5a. CONTRACT NUMBER
Scramjet Flow Field Control Using Magnetogasdynamics	
	5b. GRANT NUMBER
	5c. PROGRAM ELEMENT NUMBER

6. AUTHOR(S)	5d. PROJECT NUMBER
McMullan Richard J., Maj, USAF	2003-014
	5e. TASK NUMBER
	5f. WORK UNIT NUMBER

7. PERFORMING ORGANIZATION NAME(S) AND ADDRESS(ES)	8. PERFORMING ORGANIZATION REPORT NUMBER
Air Force Institute of Technology Graduate School of Engineering and Management (AFIT/EN) 2950 Hobson Way WPAFB OH 45433-7765	

9. SPONSORING / MONITORING AGENCY NAME(S) AND ADDRESS(ES)	10. SPONSOR/MONITOR'S ACRONYM(S)
AFOSR/NA Dr. John Schmisseur 875 N. Randolph Street Suite 325, Room 3112 Arlington, VA 22203 (703) 696-6962	
	11. SPONSOR/MONITOR'S REPORT NUMBER(S)

12. DISTRIBUTION / AVAILABILITY STATEMENT

Approved for public release; distribution unlimited.

13. SUPPLEMENTARY NOTES

14. ABSTRACT

Sustained hypersonic flight using scramjet propulsion is the key technology bridging the gap between turbojets and the exoatmospheric environment where a rocket is required. Recent efforts have focused on electromagnetic (EM) flow control to mitigate the problems of high thermomechanical loads and low propulsion efficiencies associated with scramjet propulsion. Numerical simulations were employed to determine how EM flow control can improve scramjet performance. The research effort focused on applying both local flow field control and the system level magnetogasdynamic (MGD) energy bypass method to a flight-scale scramjet. This report highlights the major accomplishments of this research effort. Combustor-based MGD generators proved superior to inlet generators with respect to power density and overall engine efficiency. MGD acceleration was shown to be ineffective in improving overall performance with all of the bypass engines having approximately 33% more drag than baseline engine without EM flow control, and none of them achieved a self-powered state.

15. SUBJECT TERMS

Supersonic Combustion Ramjet Engines, Magnetogasdynamics, Computational Fluid Dynamics, Hypersonic Vehicles

16. SECURITY CLASSIFICATION OF:			17. LIMITATION OF ABSTRACT	18. NUMBER OF PAGES	19a. NAME OF RESPONSIBLE PERSON
a. REPORT	b. ABSTRACT	c. THIS PAGE			Richard J. McMullan (ENY)
U	U	U	UU	102	19b. TELEPHONE NUMBER *(include area code)* (937) 255–3636, ext 4578